

**Highlight 1.** *A new thin-film ThermoMesh that simultaneously senses and compresses a spatio-temporally sparse temperature signal passively using phonon and electron transport.*

**Highlight 2.** *Performance characteristics (range, efficiency, sensitivity, and accuracy) are defined and derived based on an experimentally validated model to arrive at practical designs for both contact and non-contact conduction-based thermal imaging systems.*

**Highlight 3.** *The new sensor promises orders of magnitude improvement in energy efficiency for the measurement of extremely rare thermal events that are sparse in both space and time.*

# Design and Characteristics of a Thin-Film ThermoMesh for the Efficient Embedded Sensing of a Spatio-Temporally Sparse Heat Source

Sajjad Boorghan Farahan

*Department of Mechanical Engineering  
State University of New York at Binghamton, Binghamton, NY*

Ahmed Alajlouni

*Department of Mechanical Engineering  
State University of New York at Binghamton, Binghamton, NY*

Jingzhou Zhao\*

*Department of Mechanical Engineering  
State University of New York at Binghamton, Binghamton, NY*

---

## Abstract

This work presents ThermoMesh, a passive thin-film thermoelectric mesh sensor designed to detect and characterize spatio-temporally sparse heat sources through conduction-based thermal imaging. The device integrates thermoelectric junctions with linear or nonlinear interlayer resistive elements to perform simultaneous sensing and in-sensor compression. We focus on the single-event (1-sparse) operation and define four performance metrics: range, efficiency, sensitivity, and accuracy. Numerical modeling shows that a linear resistive interlayer flattens the sensitivity distribution and improves minimum sensitivity by approximately tenfold for a  $16 \times 16$  mesh. Nonlinear temperature-dependent interlayers further enhance minimum sensitivity at scale: a ceramic negative-temperature-coefficient (NTC) layer over 973–1273 K yields a  $\sim 14,500\times$  higher minimum sensitivity than the linear design at a  $200 \times 200$  mesh, while a  $\text{VO}_2$  interlayer modeled across its metal–insulator

---

\*Corresponding author

*Email address:* [jingzhou.zhao@binghamton.edu](mailto:jingzhou.zhao@binghamton.edu) (Jingzhou Zhao\*)

transition (MIT) over 298–373 K yields a  $\sim 24\times$  improvement. Using synthetic 1-sparse datasets with white boundary-channel noise at a signal-to-noise ratio of 40 dB, the VO<sub>2</sub> case achieved 98% localization accuracy, a mean absolute temperature error of 0.23 K, and a noise-equivalent temperature (NET) of 0.07 K. For the ceramic-NTC case no localization errors were observed under the tested conditions, with a mean absolute temperature error of 1.83 K and a NET of 1.49 K. These results indicate that ThermoMesh could enable energy-efficient embedded thermal sensing in scenarios where conventional infrared imaging is limited, such as molten-droplet detection or hot-spot monitoring in harsh environments.

*Keywords:*

Thin-Film Sensor; Localization; In-sensor Compression; Embedded Sensing; Rare-Event Detection

---

## 1. Introduction and Background

Many context-specific imaging tasks (e.g., localization, anomaly detection, pattern recognition, etc.) benefit from signal compression in the physical, analog, or digital domain [1, 2, 3, 4] to achieve significant performance improvements at the system level. This has been successfully demonstrated for magnetic [5], tactile [6, 7, 8, 9, 10], acoustic [11], electromagnetic [12, 13], and optical [14] imaging, to name a few. However, very few works [15, 16] have been proposed or reported to date that perform in-sensor compression based on phonon and electron transport for applications that require conduction-based thermal imaging, presenting a significant untapped potential.

Conduction-based thermal imaging systems typically rely on the minute diffusion length or thermal mass of a thin-film to achieve the desired temporal resolution in both contact [17, 18, 19, 20, 21, 22, 23, 24, 25, 26] and non-contact [27] use cases. Employing the emerging physical in-sensor computing [3] and compression [14] concepts promises new designs with enlarged sensing area, reduced power consumption, and simplified readout circuitry for many high-stakes applications that require the timely measurement of a rare or spatio-temporally sparse temperature signal, such as the detection of Lithium-ion battery thermal runaway [28, 29], monitoring of laser- and particle-based thermal processes [30, 31], detection of spatio-temporally resolved hot-spot in microelectronics [32, 33], understanding of laminar-turbulent boundary layer transition [34, 35], bolometer-based radar [36], detection of solar-flare,

and artificial thermal nociceptors, etc. Using sparsity explicitly as a design prior is well-motivated because sparse representations are widely studied as an efficient strategy for encoding structured signals [37].

To this end, we propose an analog–digital thin-film thermal mesh sensor (i.e., ThermoMesh) that utilizes thermoelectric and thermally responsive nonlinear resistive elements (e.g., thermal switches or thermistors) to perform simultaneous sensing and computing passively in the physical domain, with read-only resistive memories programmed into the structure and material properties of the device at the manufacturing stage. Using an experimentally validated model [15] adapted to this new design, we progressively arrive at acceptable performance characteristics for practically measuring the location and magnitude of spatio-temporally sparse temperature signals (e.g., generated by a small and fast-moving molten metal droplet both before and after impact [38]).

Section 2 defines the ThermoMesh architecture and performance metrics, and reports methods and results for linear and nonlinear interlayer designs. Section 3 provides an in-depth discussion of design implications, limitations, and potential for broader integration. Finally, Section 4 concludes the paper and outlines future directions, including fabrication, experimental validation, and potential applications.

## 2. System Design and Performance Characteristics

In this section, we present the main methods and results of this work, divided into four parts. First, we define the discrete ThermoMesh measurement model—showing how it *simultaneously senses and compresses* spatio-temporally sparse inputs—by defining the sensitivity matrix  $\mathbf{A}$  that maps the interior temperature vector  $\mathbf{T}$  to the perimeter boundary-voltage vector  $\mathbf{V}$ , and we summarize the performance metrics used throughout (i.e., range, efficiency, sensitivity, and accuracy). Second, we present an analog–digital thin-film sensing architecture for 2D heat-source localization and temperature estimation under a single-pixel operating regime, which motivates the ideal-switch interpretation and the interlayer variants studied in this paper. Third, we assemble the *linear* sensing matrix and analyze its properties, quantifying per-junction and minimum sensitivities and studying how a temperature-independent interlayer resistance reshapes the sensitivity distribution. Finally, we extend the model by incorporating a *temperature-dependent* interlayer (e.g., negative-temperature-coefficient (NTC) materials), for which the mapping

becomes state dependent; we evaluate its impact on minimum sensitivity and super-linear behavior across operating temperatures.

### 2.1. Sensor designs and performance metrics

The ThermoMesh sensor is composed of thermocouple wires assembled (or welded, printed, deposited, etc.) in a wire mesh configuration. Their crossings form thermocouple junctions, which are the physical temperature-sensing sites of the device and are assumed to be in thermal equilibrium with the measurand. When the sensor is viewed as an imaging array, each sensing junction is treated as one pixel. By contrast, in the electrical network model, a node denotes an electrical unknown used in the Kirchhoff current law (KCL) formulation. Temperature differences between adjacent junctions generate thermoelectric electromotive force (EMF) in the thermocouple wires (Chromel and Alumel for K-type thermocouples) due to the Seebeck effect. The wire segments connecting adjacent nodes can therefore be considered as voltage sources with internal resistance, whose EMF is determined by the temperature difference and the Seebeck coefficient of the wires between adjacent nodes. Fig. 1 summarizes the three interlayer variants analyzed in this work. In the figure, the top-layer patch is a gold pad used only as an optical transducer for laser-based characterization.

We work with a discrete temperature signal defined on the junction grid. Let the array have  $M$  rows and  $N$  columns of junctions, and let  $n = 1, 2, \dots$  index discrete sampling times  $t_n$ . The temperature at junction  $(i, j)$  and frame  $n$  is denoted

$$T_{i,j}[n], \quad i = 1, \dots, M, \quad j = 1, \dots, N, \quad (1)$$

and we collect all  $MN$  junction temperatures at frame  $n$  into a column vector

$$\mathbf{T}[n] = [T_{1,1}[n], \dots, T_{1,N}[n], T_{2,1}[n], \dots, T_{M,N}[n]]^T \in \mathbb{R}^{MN}. \quad (2)$$

This  $\mathbf{T}[n]$  is the discrete temperature signal that the sensor is designed to measure at frame  $n$ . A reconstruction method produces an estimate  $\hat{\mathbf{T}}[n]$  from the measured boundary voltages; later sections evaluate performance by comparing  $\hat{\mathbf{T}}[n]$  with  $\mathbf{T}[n]$ .

At each frame, the exterior boundary voltages are collected into a vector

$$\mathbf{V}[n] = [V_1[n], \dots, V_{2M+2N}[n]]^T \in \mathbb{R}^{2M+2N}, \quad (3)$$

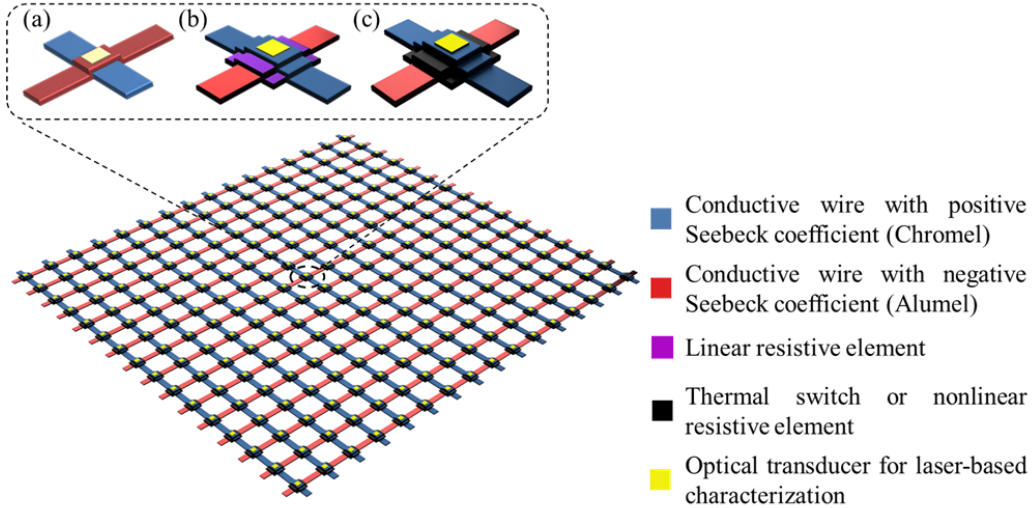


Figure 1: **ThermoMesh physical architecture and interlayer variants.** A mesh of orthogonal **Chromel** and **AlumeL** lines forms an array of thermocouple junctions. The inset highlights three junction configurations considered in this work: (a) a direct metal–metal crossing without an added interlayer, (b) insertion of a temperature-independent resistive interlayer yielding linear behavior, and (c) incorporation of a temperature-dependent interlayer that produces nonlinear or switch-like behavior.

where the index runs over all boundary channels on the perimeter of the mesh. For a given ThermoMesh design, the relationship between  $\mathbf{V}[n]$  and  $\mathbf{T}[n]$  is obtained from a network model. In the linear (temperature-independent) case this is a matrix–vector product

$$\mathbf{V}[n] = \mathbf{A} \mathbf{T}[n], \quad \mathbf{A} \in \mathbb{R}^{(2M+2N) \times (MN)}, \quad (4)$$

where  $\mathbf{A}$  is the *sensitivity matrix* that maps the interior temperature vector to the measured boundary-voltage vector. With a temperature-dependent interlayer, the coefficients of  $\mathbf{A}$  depend on the operating temperatures, and the measurement model becomes

$$\mathbf{V}[n] = \mathbf{A}(\mathbf{T}[n]) \mathbf{T}[n]. \quad (5)$$

These relations hold independently at each time stamp  $t_n$  as long as charge transport is much faster than heat transport. In the parallel-plate limit, the RC time constant of each junction is approximately equal to  $\rho \varepsilon_0 \varepsilon_r$ , where  $\rho$  is the interlayer resistivity,  $\varepsilon_r$  is the interlayer relative permittivity,

and  $\varepsilon_0$  is the permittivity of free space. It is therefore independent of pixel dimensions and interlayer geometry and is set primarily by material properties. For the interlayer materials considered in this work, it is estimated to be smaller than  $1 \mu\text{s}$ , so its effect on response time is neglected in the present model; by contrast, materials with much larger resistivity and permittivity (e.g., pyroelectric materials) could yield a larger RC time constant and correspondingly slower response.

The matrix  $\mathbf{A}$  is computed by applying KCL to the network and using the wire and interlayer material relations. For clarity, we consider the 3D stack indexed by  $(i, j, k)$  for row, column, and layer. At each interior node  $(i, j, k)$ , KCL gives

$$\begin{aligned}
& G_{i,j,k;i-1,j,k}(U_{i,j,k} - U_{i-1,j,k}) + G_{i,j,k;i+1,j,k}(U_{i,j,k} - U_{i+1,j,k}) \\
& + G_{i,j,k;i,j-1,k}(U_{i,j,k} - U_{i,j-1,k}) + G_{i,j,k;i,j+1,k}(U_{i,j,k} - U_{i,j+1,k}) \\
& + G_{i,j,k;i,j,k-1}(U_{i,j,k} - U_{i,j,k-1}) + G_{i,j,k;i,j,k+1}(U_{i,j,k} - U_{i,j,k+1}) \quad (6) \\
= & -S_{i,j,k;i-1,j,k}(T_{i,j} - T_{i-1,j}) - S_{i,j,k;i+1,j,k}(T_{i,j} - T_{i+1,j}) \\
& -S_{i,j,k;i,j-1,k}(T_{i,j} - T_{i,j-1}) - S_{i,j,k;i,j+1,k}(T_{i,j} - T_{i,j+1})
\end{aligned}$$

where  $G$ . are inter-node conductances,  $S$ . are the effective Seebeck couplings,  $U_{i,j,k}$  is the electric potential of node  $(i, j, k)$ , and  $T_{i,j,k}$  is the corresponding junction temperature relative to the cold junction. Peltier and Thomson effects are neglected assuming small currents ( $<1 \mu\text{A}$ ). In matrix form the interior-node potentials  $\mathbf{U}$  and temperatures  $\mathbf{T}$  satisfy

$$\mathbf{G}\mathbf{U} = \mathbf{S}\mathbf{T}, \quad (7)$$

with  $\mathbf{G}$  the conductance matrix and  $\mathbf{S}$  the Seebeck-coefficient matrix. The boundary voltages are obtained from the solved node potentials and Seebeck sources via selection matrices  $\mathbf{I}_U$ ,  $\mathbf{I}_S$ , and  $\mathbf{I}_V$ ,

$$\mathbf{V} = (\mathbf{I}_U \mathbf{G}^{-1} \mathbf{S} + \mathbf{I}_S + \mathbf{I}_V) \mathbf{T} \triangleq \mathbf{A} \mathbf{T}, \quad (8)$$

where  $\mathbf{I}_U$  selects the contributions of the interior-node potentials at the measured boundary channels,  $\mathbf{I}_S$  selects the Seebeck contributions applied directly at the boundary channels, and  $\mathbf{I}_V$  enforces the measurement reference used by the readout electronics (i.e., voltages are defined relative to a chosen datum). This reference is required because the network can be electrically

floating, in which case the absolute potentials are only defined up to an additive constant;  $\mathbf{I}_V$  fixes that gauge without changing physically meaningful voltage differences. The resulting boundary voltages were also verified by circuit-level simulation of the ThermoMesh network in LTspice. Together, Eqs. (4)–(8) define the ThermoMesh measurement model.

For each frame  $n$ , the *spatial sparsity* of the temperature signal is the number of nonzero entries in  $\mathbf{T}[n]$ ,

$$\|\mathbf{T}[n]\|_0 \triangleq \#\{j : T_j[n] \neq 0\}, \quad (9)$$

where  $j$  indexes the  $MN$  junctions. Over an observation sequence, the *temporal sparsity* is defined as

$$q_t \triangleq \max_n \|\mathbf{T}[n]\|_0, \quad (10)$$

i.e., the largest number of simultaneously active junctions in any single frame of that sequence; this is equivalently the largest number of simultaneous events in any frame of the sequence.

We define the *event duration*  $\tau_e$  as the time interval during which a heat source remains detectable somewhere within the sensing area, including motion, ending when it exits the measurement region or cools below detectability.

The sparse-event regime considered in this work assumes scale separation in both time and space. Let  $\tau_m$  denote the measurement-window duration,  $\tau_e$  the event duration defined above, and  $\tau_s$  the pixel characteristic heat-transfer (thermal equilibration) time constant. Thin-film non-contact operation can achieve  $\tau_s$  down to about 100  $\mu\text{s}$  in thermal-mass-limited designs [39], whereas contact operation can achieve  $\tau_s$  down to about 50 ns in thermal-diffusion-limited designs [40]. The temporal sparse-event regime assumed here therefore requires  $\tau_m \gg \tau_e \gg \tau_s$ . Spatially, we distinguish the total sensor area  $A_s$ , the pixel area  $A_p$ , and the event footprint area  $A_e$ . We assume  $A_s \gg A_p$  and that a single event excites at most one pixel within a given frame. Equivalently, the event must not raise neighboring pixels above detectability. Under this assumption, multi-pixel excitation by a single localized event is not considered in the present work.

We define four performance metrics: *range*, *efficiency*, *sensitivity*, and *accuracy*.

### 2.1.1. Range

In this work, *range* refers to the operating regimes over which the sensor and the associated reconstruction are specified and characterized. In addi-

tion to the conventional temperature operating range, we also characterize a *sparsity range*, which is specific to the proposed in-sensor compression framework.

The *temperature range* is the interval  $[T_{\min}, T_{\max}]$  of junction temperatures over which the sensor and reconstruction are specified and characterized.

For a given design and reconstruction method, the sensor is *characterized up to spatial sparsity*  $q_s^{\max}$  if its performance has been characterized for all frames satisfying  $\|\mathbf{T}[n]\|_0 \leq q_s^{\max}$ . The set

$$\{0, 1, \dots, q_s^{\max}\} \quad (11)$$

is then the *spatial sparsity range* of the sensor.

Likewise, the sensor is *characterized up to temporal sparsity*  $q_t^{\max}$  if its performance has been characterized for all observation sequences satisfying  $q_t \leq q_t^{\max}$ . The set

$$\{0, 1, \dots, q_t^{\max}\} \quad (12)$$

is then the *temporal sparsity range* of the sensor.

In this work we focus on  $q_s^{\max} = 1$  and  $q_t^{\max} = 1$ .

### 2.1.2. Efficiency

*Efficiency* measures the dynamic readout energy per frame. Let  $E_s$  denote the energy required by the readout electronics (e.g., analog front-end and ADC/DAQ) to acquire one boundary-channel voltage sample. Then the ADC energy per frame scales with the number of readout channels:

$$E_{\text{frame}} \propto N_{\text{read}} E_s. \quad (13)$$

Let  $N_{\text{pix}}$  denote the total number of pixels and  $N_{\text{read}}$  denote the number of readout channels. A conventional imager reads all pixels and therefore uses  $N_{\text{pix}}$  readout channels, whereas ThermoMesh uses only  $N_{\text{read}}$  boundary channels. The resulting channel-count reduction factor is

$$\eta_{\text{ch}} = \frac{N_{\text{pix}}}{N_{\text{read}}}. \quad (14)$$

Because ThermoMesh uses perimeter-only readout,  $N_{\text{read}}$  scales with the linear dimension of the array. Equivalently, Eq. (14) scales linearly with  $\sqrt{N_{\text{pix}}}$ , i.e., with the square root of the number of pixels assuming a square sensing area.

### 2.1.3. Sensitivity

*Sensitivity* is characterized by the boundary–voltage swing generated by a unit temperature increase at interior junction  $j$ ,

$$\sigma_j = \max_i A_{ij} - \min_i A_{ij} \quad [\text{V/K}], \quad (15)$$

and by the minimum sensitivity across the array,

$$\sigma_{\min} = \min_j \sigma_j. \quad (16)$$

To quantify nonlinearity we follow the log–log slope metric used for super-linear sensor response [3], where super-linearity is defined with respect to output magnitude and stimulus intensity. In the nonlinear-interlayer case, the sensing matrix depends on temperature, so the boundary response depends on the stimulus level. We therefore fix the ambient temperature at  $T_{\text{amb}}$  and heat a specific junction (the center) by an amount  $\Delta T$  above the ambient temperature. Let  $\Delta V_{\text{center}}(\Delta T)|_{T=T_{\text{amb}}}$  denote the resulting boundary–voltage swing. Following the log–log slope metric used for super-linear sensor response [3], we define the super-linearity exponent

$$\kappa(\Delta T)|_{T=T_{\text{amb}}} = \frac{d \ln \Delta V_{\text{center}}(\Delta T)|_{T=T_{\text{amb}}}}{d \ln \Delta T} \quad (17)$$

so that  $\kappa > 1$  indicates a super-linear increase of boundary response with stimulus amplitude.

### 2.1.4. Accuracy

Accuracy is evaluated at two levels. At the task level, heat-source *localization* is treated as a *classification* problem (one class per pixel), and temperature *estimation* is treated as a *regression* problem.

For localization, each pixel is assigned a unique class index  $c \in \{1, \dots, MN\}$  using the same indexing as in the dataset. Let  $N_{\text{eval}}$  denote the number of evaluation samples, and let  $c_n$  and  $\hat{c}_n$  denote the ground-truth and predicted class indices for sample  $n \in \{1, \dots, N_{\text{eval}}\}$ . Localization accuracy is defined as

$$\text{Acc} = \frac{1}{N_{\text{eval}}} \sum_{n=1}^{N_{\text{eval}}} \mathbf{1}\{\hat{c}_n = c_n\}, \quad (18)$$

where  $\mathbf{1}\{\cdot\}$  is the indicator function.

To quantify localization errors when  $\hat{c}_n \neq c_n$ , we map each class index  $c$  to its 2D pixel location  $\boldsymbol{\phi}(c) = (x_c, y_c)$  on the  $M \times N$  grid using the same class-to-location mapping as in the dataset. The (per-sample) normalized spatial error is

$$d_{\text{norm}}(n) = \frac{\|\boldsymbol{\phi}(\hat{c}_n) - \boldsymbol{\phi}(c_n)\|_2}{\sqrt{(M-1)^2 + (N-1)^2}}, \quad (19)$$

i.e., Euclidean pixel distance normalized by the mesh diagonal.

For temperature estimation, let  $T_n$  and  $\hat{T}_n$  denote the ground-truth and predicted temperatures for sample  $n$ . The mean absolute error (MAE) is

$$\text{MAE} = \frac{1}{N_{\text{eval}}} \sum_{n=1}^{N_{\text{eval}}} |\hat{T}_n - T_n|. \quad (20)$$

For the device-level evaluation, we report the noise-equivalent temperature (NET),

$$\text{NET} \approx \frac{\text{std}(\boldsymbol{\nu})}{\|\Delta \mathbf{V} / \Delta T\|}, \quad (21)$$

where  $\boldsymbol{\nu}$  is the boundary-voltage noise vector,  $\text{std}(\boldsymbol{\nu})$  denotes the standard deviation computed across the boundary channels, and  $\|\Delta \mathbf{V} / \Delta T\|$  is an aggregate sensitivity. NET summarizes the temperature change that produces a boundary-voltage change comparable to the boundary-noise level.

## 2.2. An Analog–Digital Thin-Film Thermal Sensor for 2D Heat-Source Localization and Strength Estimation

We apply the ThermoMesh measurement model to the *single-pixel, single-event* operating regime ( $q_s^{\text{max}} = 1$ ,  $q_t^{\text{max}} = 1$ ) used throughout this paper. Consider a single discrete frame  $n$  and the corresponding junction-temperature vector  $\mathbf{T}[n] \in \mathbb{R}^{MN}$  defined on the  $M \times N$  grid. A *single localized heating event* in this framework means that, at that frame, at most one sensing junction (equivalently, one pixel) exhibits a nonzero temperature rise relative to the reference, i.e.,

$$\mathbf{T}[n] \in \mathbb{R}^{MN}, \quad T_{r^*, c^*}[n] = \Delta T[n], \quad T_{i, j}[n] = 0 \text{ for } (i, j) \neq (r^*, c^*), \quad (22)$$

where  $(r^*, c^*)$  denotes the row and column indices of the active (heated) junction and  $\Delta T[n]$  is its amplitude on the junction grid. Physically, under the sparse-event scale separations introduced in Section 2.1, this regime

corresponds to sufficiently localized heating such that neighboring junctions do not show a noticeable temperature rise within the same frame.

In the idealized temperature-dependent interlayer limit, each crossing behaves as a *thermal switch* with resistance

$$R(T) = \begin{cases} 0, & T \geq T_{\text{th}}, \\ \infty, & T < T_{\text{th}}, \end{cases} \quad (23)$$

so only the heated junction  $(r^*, c^*)$  closes while all other crossings remain open. Here  $T_{\text{th}}$  is the switching threshold at which the interlayer transitions from the high-resistance (open) state to the low-resistance (closed) state. Under this ideal-switch behavior, the boundary measurement vector  $\mathbf{V}[n]$  contains a *digital* location signature and an *analog* magnitude: the boundary channels that are electrically connected to the closed row and column exhibit defined voltages relative to the measurement reference, and their indices identify the active row and column (and thus the 2D location  $(r^*, c^*)$ ), while their magnitudes depend on  $\Delta T[n]$  through the effective Seebeck coefficients and the network conductances. Boundary channels with no conductive path to the closed junction are electrically floating (open-circuit) under this ideal model and do not carry location information. An equivalent-circuit schematic—showing the boundary channels, internal node potentials, and junction temperatures—is provided in Fig. 2.

A perfect thermal switch that satisfies all design constraints is not always available in practice. Accordingly, the remainder of the paper analyzes three interlayer realizations introduced in Fig. 1: (i) *baseline (no interlayer)* [15], in which only the native thermocouple junction is present; (ii) a *constant-resistance interlayer (linear)*, where the interlayer behaves as a temperature-independent resistor; and (iii) a *temperature-dependent interlayer (nonlinear)*, where the interlayer resistance depends on temperature.

### 2.3. ThermoMesh with Linear Resistance Interlayer

We begin from the baseline ThermoMesh containing only crossed thermocouple wires and no resistive interlayer. Its 2D equivalent circuit, used to assemble the linear measurement model in Eq. (4), is shown in Fig. 3. In this configuration the boundary channels are measured to form the voltage vector  $\mathbf{V}$ ; interior temperatures are reconstructed from the boundary measurements.

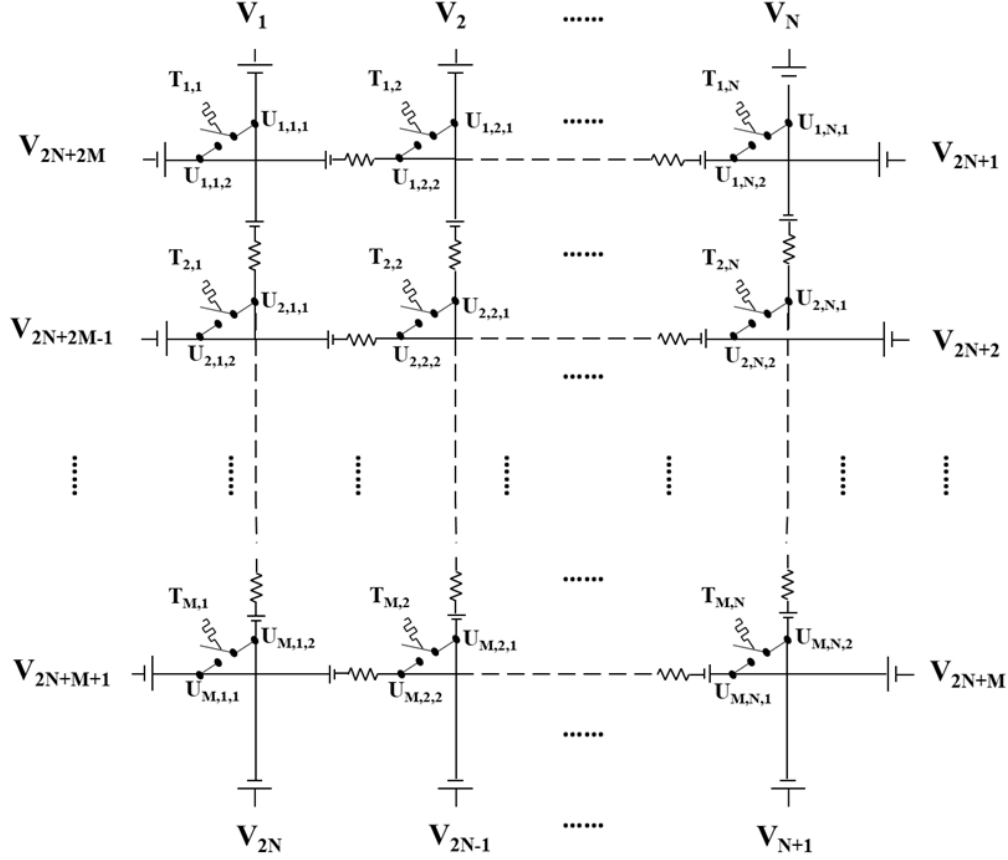


Figure 2: Ideal-switch equivalent circuit.

The baseline sensitivity is strongly edge-biased. The weakest region (near the center) has sensitivity well below the K-type thermocouple typical value ( $\sim 40 \mu\text{V/K}$ ), which limits detection near the middle of the mesh. To mitigate this while preserving the linear model in Eq. (4), we introduce a thin *linear resistive interlayer* between the stacked films. Electrically, this adds temperature-independent shunt paths at each crossing and reshapes the sensitivity matrix while keeping the model linear. The modified circuit used in subsequent calculations is shown in Fig. 4. In the linear case, the temperature range is set primarily by the thermocouple material rather than the interlayer; for K-type thermocouples, it is on the order of 1600 K.

Uniqueness of sparse recovery in the linear-interlayer case is assessed via the Null Space Property (NSP): if the sensitivity matrix  $\mathbf{A}$  satisfies

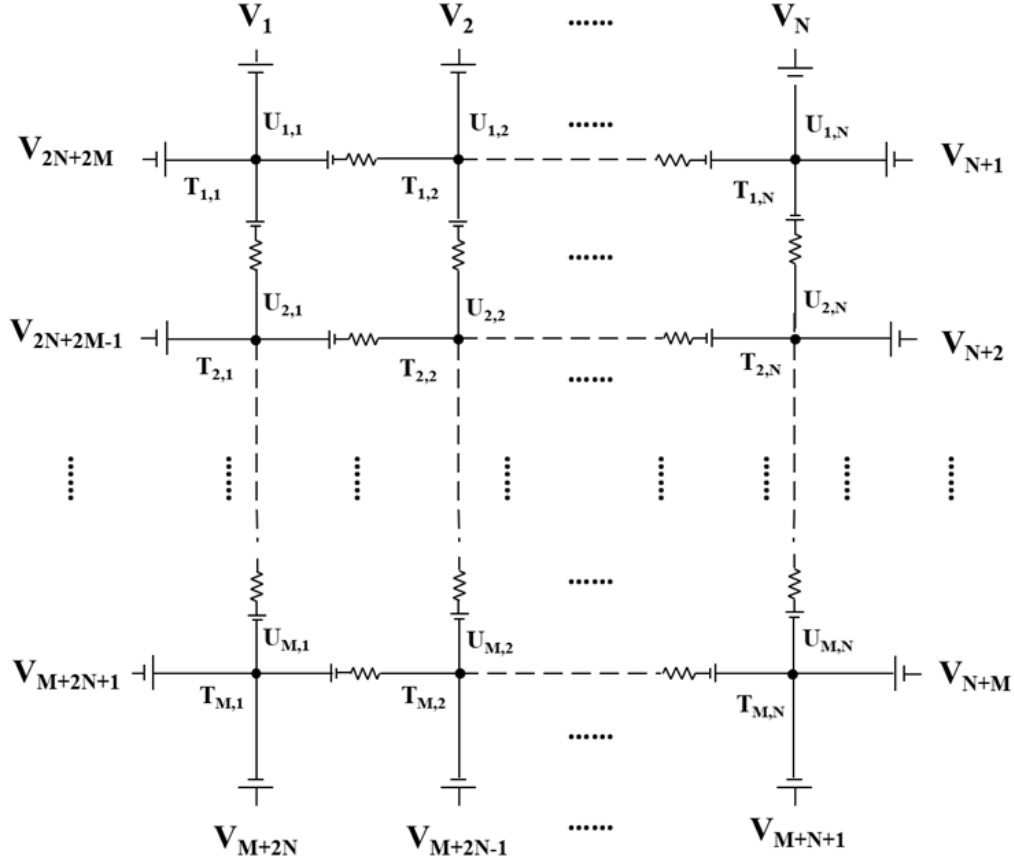


Figure 3: Equivalent circuit used to represent the baseline ThermoMesh (no interlayer).

the NSP of order  $q_s^{\max}$ , then any temperature field  $\mathbf{T}$  with  $\|\mathbf{T}\|_0 \leq q_s^{\max}$  is uniquely determined by the measured boundary voltages  $\mathbf{V}$ . We verified that the sensitivity matrices  $\mathbf{A}$  assembled from the network satisfy the NSP for  $q_s^{\max} = 1$  across multiple array sizes (up to  $200 \times 200$ ). Therefore, in the linear case, a 1-sparse temperature field is uniquely determined by the boundary measurements, and this is consistent with the Orthogonal Matching Pursuit (OMP) recovery results reported later in this subsection.

Per-junction sensitivity  $\sigma_j$  and minimum sensitivity  $\sigma_{\min}$  are computed using the definitions given once in Section 2.1 (Eqs. (15)–(16)); because the interlayer is temperature independent,  $\sigma_j$  and  $\sigma_{\min}$  are temperature independent for a fixed geometry and materials set.

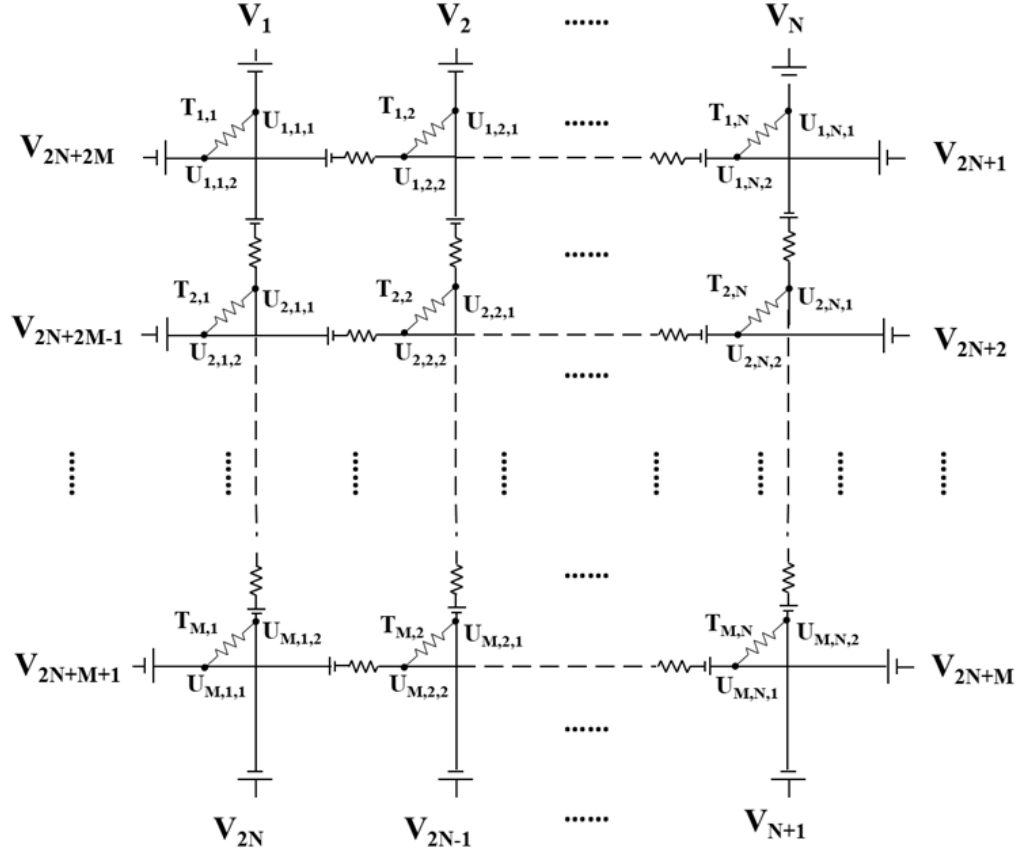


Figure 4: Equivalent circuit of ThermoMesh with a linear resistive interlayer.

The effect of the linear interlayer on sensitivity is shown in Fig. 5 by comparing the baseline map (no interlayer) with the corresponding map obtained with the linear resistive interlayer. Panel (a) shows the baseline distribution; panel (b) shows the distribution with the linear interlayer. In both panels, the inset is a zoom of the central junctions using the *same scale and colorbar* to enable a direct comparison. With the interlayer, the minimum (central-junction) sensitivity rises from  $4.67 \times 10^{-7}$  V/K to  $4.51 \times 10^{-6}$  V/K (a  $\approx 10\times$  increase), and the profile flattens markedly. Although junctions near the boundary become less sensitive than in the baseline, the minimum sensitivity increases and the spatial distribution of sensitivity becomes substantially more uniform overall.

Treating the interlayer resistance  $R$  as a design parameter shows that the

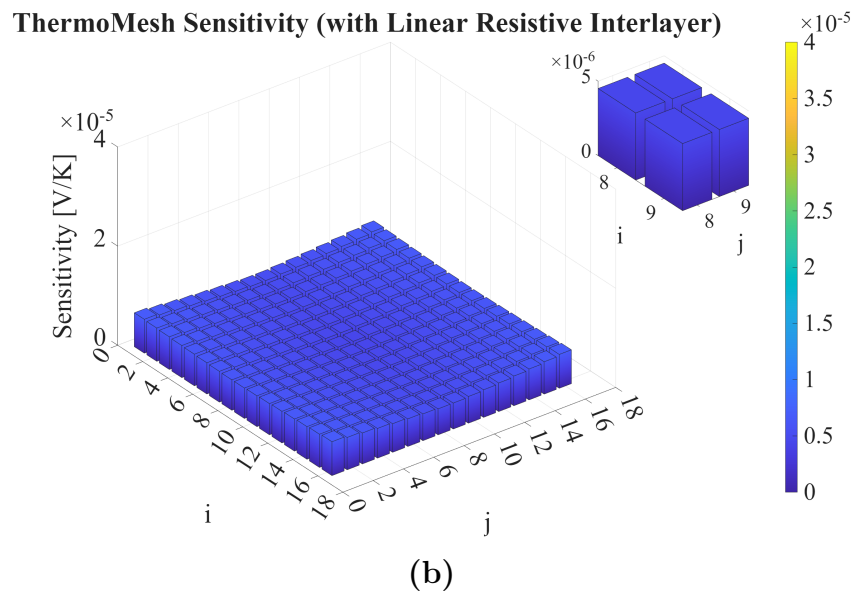
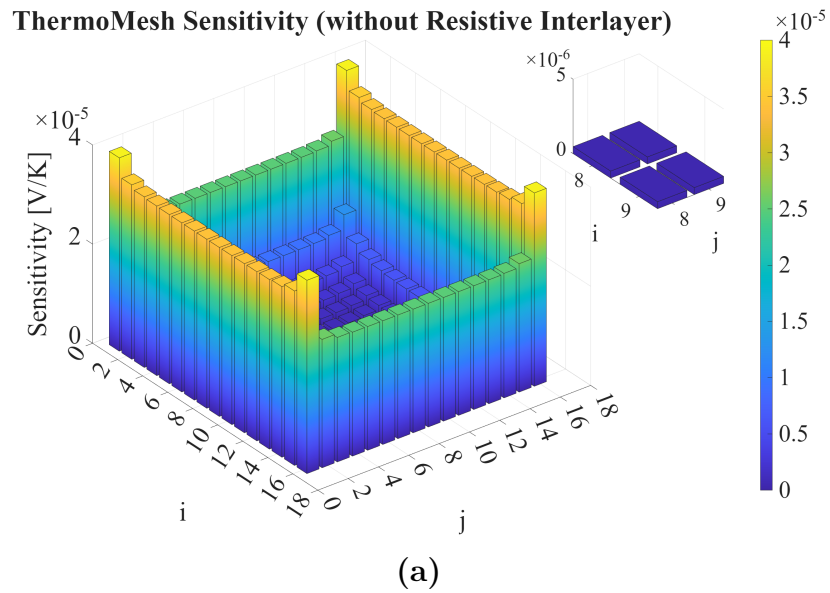


Figure 5: **Sensitivity maps for a  $16 \times 16$  ThermoMesh.** (a) Baseline configuration without a resistive interlayer, showing strong edge-dominated sensitivity and reduced response near the center. (b) Corresponding map with a linear resistive interlayer, illustrating redistribution and flattening of sensitivity across the mesh.

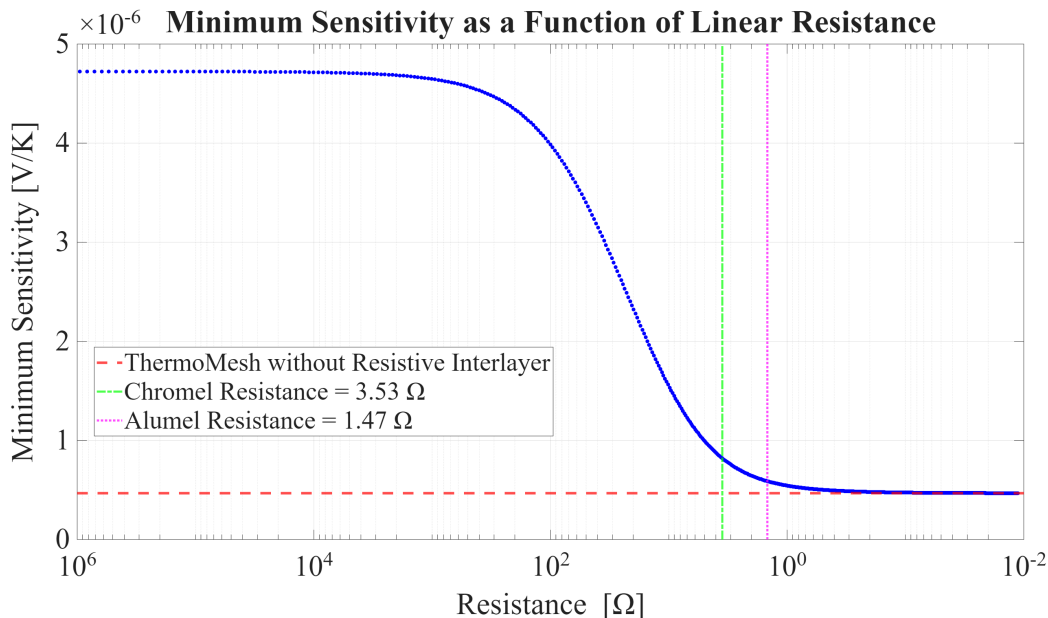


Figure 6: Minimum sensitivity versus linear interlayer resistance for a  $16 \times 16$  mesh. The dashed red line denotes the baseline (no interlayer). As  $R$  increases,  $\sigma_{\min}$  increases and approaches a high- $R$  plateau; as  $R \rightarrow 0$ , the curve returns to the baseline. Vertical dashed lines mark representative Chromel and Alumel resistances for reference.

minimum sensitivity depends strongly on  $R$ . Fig. 6 plots  $\sigma_{\min}$  for a  $16 \times 16$  mesh: as  $R$  increases,  $\sigma_{\min}$  increases relative to the no-interlayer baseline and then changes more slowly at larger  $R$ . As  $R \rightarrow 0$ , the curve approaches the baseline (dashed red), which matches the no-interlayer case. The vertical markers indicate representative resistances associated with the thermocouple legs (Chromel and Alumel), showing where practical values fall relative to the transition region.

Scaling the mesh shows two consistent trends (Fig. 7). First, for each size the minimum sensitivity increases with  $R$  and then changes more slowly at higher  $R$ , with the transition occurring over an intermediate- $R$  range. Second, the high- $R$  level decreases as resolution increases, reflecting the sensitivity–resolution trade-off under boundary-only readout. Relative to the baseline, the improvement provided by the resistive interlayer increases with array size; the corresponding improvement factors are summarized in Table 1.

To assess robustness, we formed a noise-free boundary signal  $\mathbf{V}_{\text{noise-free}} = \mathbf{A}\mathbf{T}$ , computed its mean-square power  $P_s$ , chose a target signal-to-noise ratio

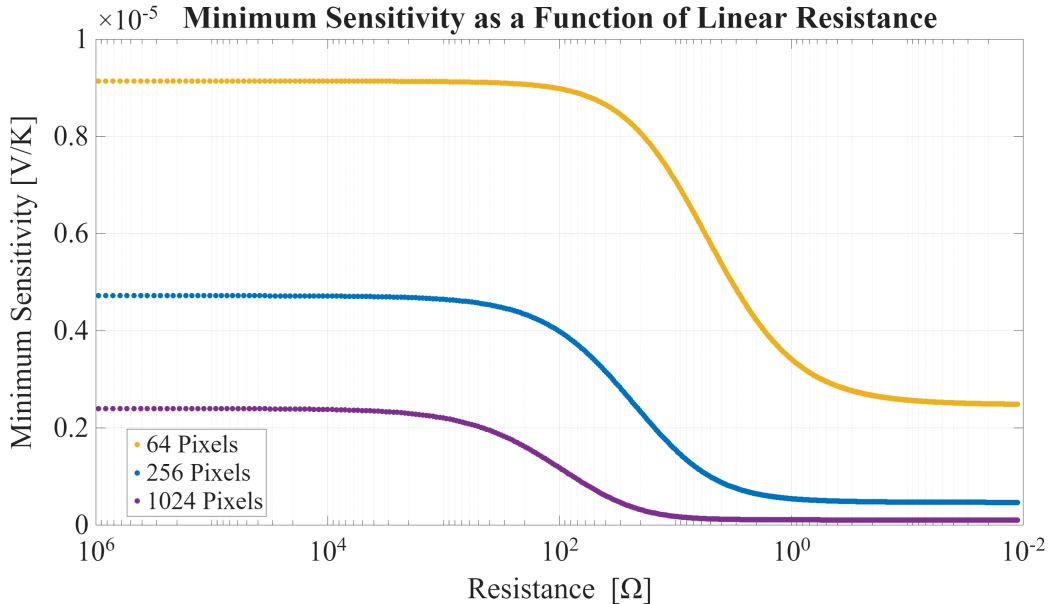


Figure 7: Minimum sensitivity versus linear interlayer resistance across mesh sizes. For each size,  $\sigma_{\min}$  increases with  $R$  and saturates at a high- $R$  plateau, while the absolute plateau decreases with increasing resolution.

( $\text{SNR}_{\text{dB}}$ ), and set the noise power to  $P_n = P_s/10^{\text{SNR}_{\text{dB}}/10}$ . We then drew a white Gaussian noise vector  $\boldsymbol{\nu} \sim \mathcal{N}(\mathbf{0}, P_n \mathbf{I})$  and formed the noisy measurements  $\mathbf{V} = \mathbf{V}_{\text{noise-free}} + \boldsymbol{\nu}$ . This models aggregate electronic/thermal disturbances as independent, zero-mean noise at the boundary channels with variance fixed by the desired SNR. Recovery was performed with OMP; success was recorded when the active junction and its amplitude were recovered. The quantitative results for  $16 \times 16$  meshgrid and  $q_s^{\max} = 1$  are listed in Table 2. Here, our goal is to illustrate noise effects; in future work we will incorporate realistic sources such as Johnson–Nyquist noise and electromagnetic interference (EMI) into the sensor-level model.

Taken together, Figs. 3–7 and Tables 1–2 show that a constant-resistance interlayer improves the minimum sensitivity and uniformity for a ThermoMesh, yet the absolute minimum sensitivity still declines with resolution. This motivates the nonlinear (temperature-dependent) interlayer studied next.

#### 2.4. ThermoMesh with Nonlinear Resistance Interlayer

A practical realization of the “thermal switch” in Fig. 2 is a *thermistor* placed between the orthogonal thermocouple films. Its resistance varies

Table 1: Minimum sensitivity improvement (relative to baseline) for the linear-interlayer design.

Mesh size ( $M \times N$ pixels)	Minimum Sensitivity Improvement
64	4×
256	10×
1024	23×

Table 2: Recovery success via OMP for the linear-interlayer design.

SNR (dB)	Recovery success rate (%)
No Noise	100
40	73
20	12

strongly with temperature but does not exhibit an ideal step change. As a result, the boundary-voltage vector is related to the junction-temperature vector through the nonlinear relation in Eq. (5), where the temperature-dependent matrix  $\mathbf{A}(\mathbf{T})$  is obtained by enforcing Kirchhoff’s current law on the network. The corresponding equivalent circuit is shown in Fig. 8.

For NTC thin films we parameterize the resistivity with the standard model,

$$\rho(T) = \rho_0 \exp\left[\beta\left(\frac{1}{T} - \frac{1}{T_0}\right)\right], \quad (24)$$

using different  $(\rho_0, \beta, T_0)$  sets appropriate to each material system. Here,  $\rho(T)$  is the interlayer *resistivity*,  $\rho_0$  is the resistivity at the reference temperature  $T_0$ , and  $\beta$  is the thermistor coefficient.  $T$  and  $T_0$  are absolute temperatures in kelvin; for NTC materials,  $\beta > 0$ , so  $\rho(T)$  decreases as  $T$  increases. For high-temperature operation we use perovskite thermistor ceramics [41]. For lower-temperature operation (e.g., bolometers), we model  $\text{VO}_2$  using a piecewise fit of Eq. (24) across the metal–insulator transition (MIT) to capture the orders-of-magnitude resistivity change [42]; recent material advances can further increase the transition sharpness and on/off ratio [43]. In ThermoMesh the temperature range  $[T_{\min}, T_{\max}]$  is therefore set primarily by the interlayer material system rather than the mesh architecture; accordingly, we report results for a  $\text{VO}_2$ –NTC interlayer over 298–373K and for a ceramic-NTC interlayer over 973–1273K.

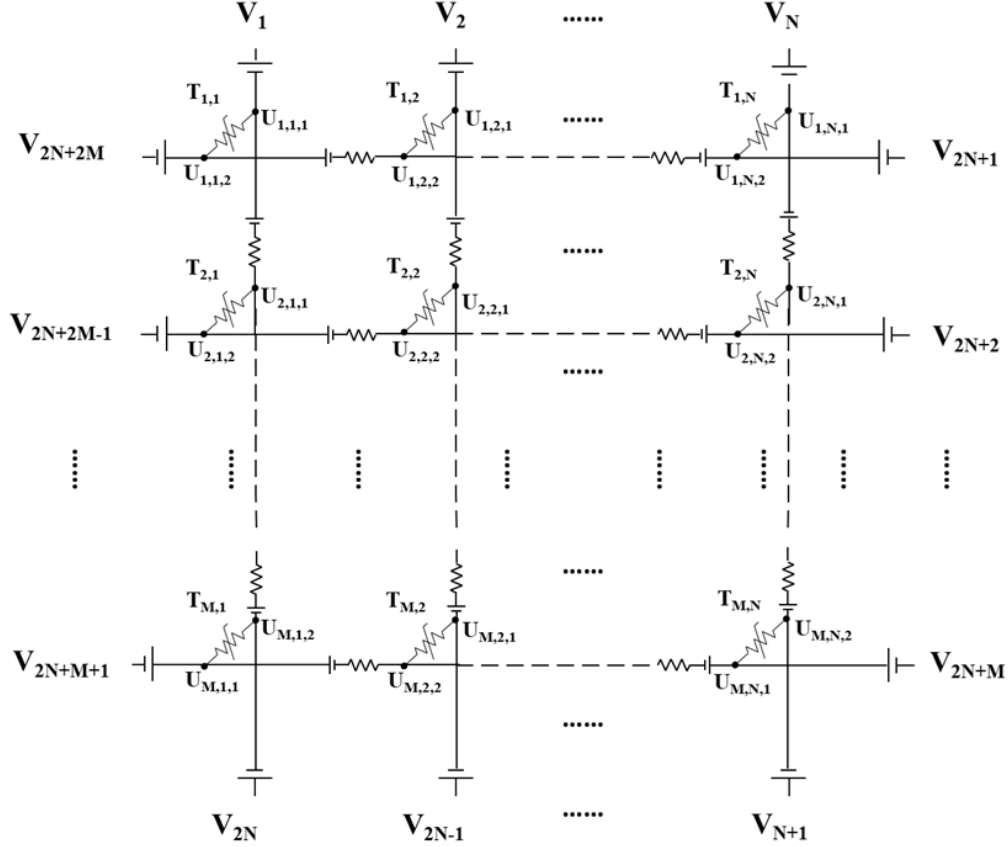


Figure 8: Equivalent circuit of ThermoMesh with a thermistor at each crossing (the interlayer).

We use the same sensitivity definitions as in the linear case (see Eqs. (15)–(16)), with the important difference that both the per-junction sensitivity and the minimum sensitivity depend on the operating temperatures. For each nonlinear dataset, we therefore report two limits: the ambient minimum sensitivity  $\sigma_{\min}^{\text{amb}} := \sigma_{\min}(\mathbf{T}_{\text{amb}})$  with all junctions at 298 K, and the event minimum sensitivity  $\sigma_{\min}^{\text{hi}} := \sigma_{\min}(\mathbf{T}_{\text{hi}})$  with one hot junction at the application temperature while the others remain at 298 K. Also, to quantify super-linear behavior we use the super-linearity exponent defined in Eq. (17), and values  $\kappa > 1$  indicate super-linear response.

We first consider a perovskite-ceramic NTC layer for extreme events such as high-temperature molten droplets: the central junction is set to 1273 K

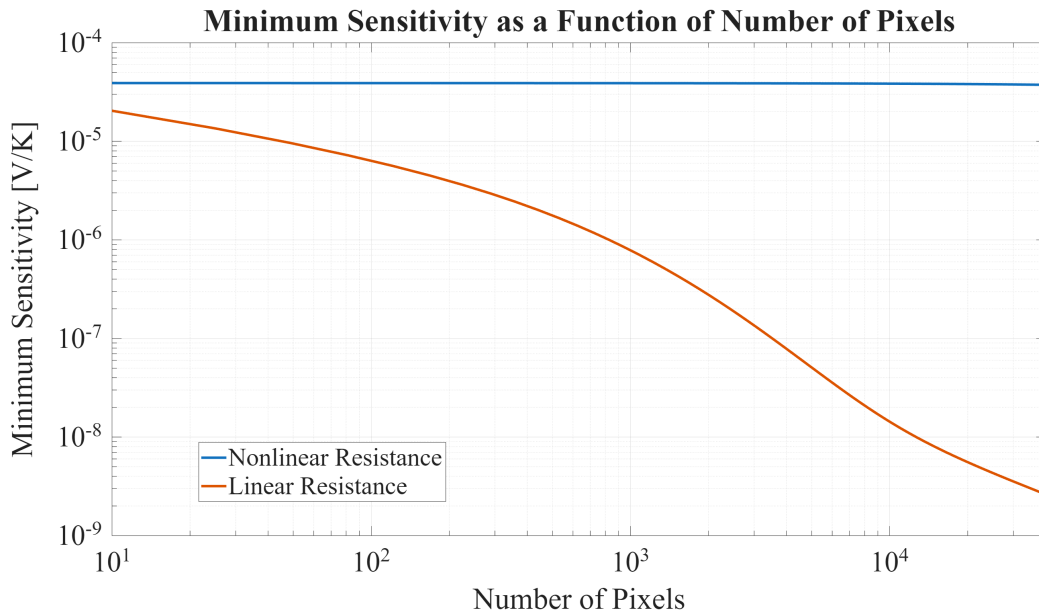


Figure 9: High-temperature case: minimum sensitivity vs. number of pixels using a ceramic-NTC interlayer compared with a linear interlayer.

while all other junctions remain at the ambient temperature. Fig. 9 plots the minimum sensitivity versus the number of pixels. The nonlinear interlayer maintains a higher minimum sensitivity as the array size increases, while the constant- $R$  case shows a much stronger decline. This is consistent with the thermal-switch interpretation: at the heated junction the interlayer resistance drops, which strengthens the coupling of the junction’s Seebeck response to the boundary readout. For the ceramic interlayer, the minimum sensitivity decreases from  $3.90 \times 10^{-5}$  V/K at 9 pixels ( $3 \times 3$ ) to  $3.70 \times 10^{-5}$  V/K at 40,000 pixels ( $200 \times 200$ ). For the linear case over the same scaling,  $\sigma_{\min}$  drops from  $2.14 \times 10^{-5}$  V/K to  $2.55 \times 10^{-9}$  V/K. Thus, for  $200 \times 200$  meshgrid the nonlinear design achieves a  $\sim 14,500\times$  higher minimum sensitivity.

For applications with lower temperatures (e.g., microbolometers), we use a  $\text{VO}_2$  interlayer and set the center to 373 K with all other junctions at the ambient temperature. Fig. 10 shows the minimum sensitivity versus pixel count for a  $\text{VO}_2$  interlayer. For a  $\text{VO}_2$  interlayer, the minimum sensitivity decreases from  $3.85 \times 10^{-5}$  V/K at 9 pixels to  $6.00 \times 10^{-8}$  V/K at 40,000 pixels, while the corresponding linear cases drop from  $1.77 \times 10^{-5}$  V/K to  $2.50 \times 10^{-9}$  V/K. For a  $200 \times 200$  meshgrid, this design yields an  $\sim 24\times$

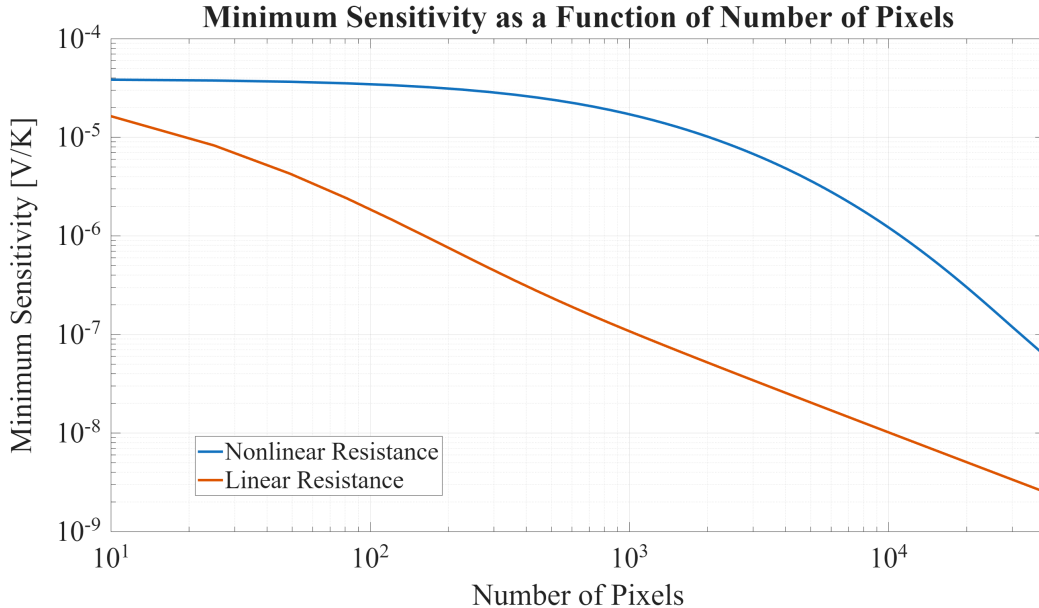


Figure 10: Low-temperature case: minimum sensitivity vs. number of pixels using a  $\text{VO}_2$  interlayer compared with a linear interlayer.

improvement in  $\sigma_{\min}$  over the linear design.

To illustrate the nonlinear behavior explicitly, we show representative curves of minimum sensitivity and super-linearity for each nonlinear material. The  $\text{VO}_2$  case exhibits a pronounced super-linear region across the MIT transition region reported in thin films [42], whereas the ceramic NTC case shows a milder but persistent super-linear response over the high-temperature range.

For the  $16 \times 16$  datasets underlying Fig. 11, we report the two limits defined above: the ambient minimum sensitivity with all junctions at 298 K, and the event minimum sensitivity when only the central junction is heated to the application temperature. For  $\text{VO}_2$ :  $\sigma_{\min}^{\text{amb}} = 4.06 \times 10^{-6} \text{ V/K}$  and  $\sigma_{\min}^{\text{hi}} = 2.91 \times 10^{-5} \text{ V/K}$  (center at 383 K). For the ceramic NTC:  $\sigma_{\min}^{\text{amb}} = 4.45 \times 10^{-6} \text{ V/K}$  and  $\sigma_{\min}^{\text{hi}} = 3.895 \times 10^{-5} \text{ V/K}$  (center at 1273 K). The corresponding super-linearity exponent  $\kappa(\Delta T)|_{T=T_{\text{amb}}}$ , extracted from the same sweeps with fixed ambient temperature, is shown in Fig. 11(c-d).

We apply machine learning algorithms for heat-source localization and temperature estimation, following the ThermoNet approach of Zhao and Ye [15]. Inputs are the boundary voltages  $\mathbf{V} \in \mathbb{R}^{2M+2N}$ ; outputs are  $MN$

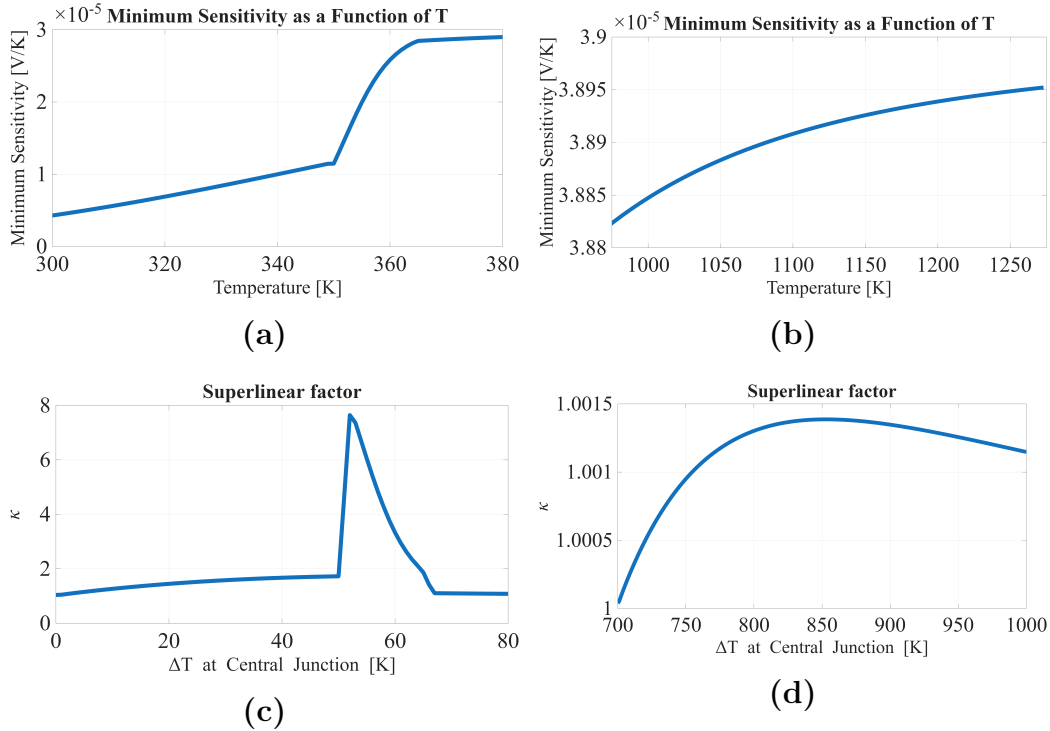


Figure 11: **Temperature-dependent behavior of nonlinear interlayers.** (a–b) Minimum sensitivity vs. heated-junction temperature for vanadium-oxide (VO<sub>2</sub>) and ceramic-NTC interlayers. (c–d) Super-linearity exponent  $\kappa(\Delta T)|_{T=T_{\text{amb}}}$  vs. hot-spot temperature rise for the same interlayers.

classes (one per pixel). We use a modified long short-term memory (LSTM) network, we use a sequence input layer, a fully connected layer, a Softmax layer, and a classification layer (cross-entropy loss). The regressor maps to the temperature via a one-hidden-layer feedforward network (30 hidden units; default mean squared error (MSE) loss). We generate synthetic 1-sparse samples from the measurement model and use a fixed split consistent with the code: 60% training, 40% validation. For the classifier we use Adam with a mini-batch size of 256 for 200 epochs.

We evaluate localization and temperature-estimation performance using the metrics defined in Section 2.1.4. Specifically, we report localization accuracy and temperature MAE across noise conditions, and we compute NET using (21). Table 3 reports localization accuracy and NET in the same format across interlayer options; Table 4 reports temperature-regression MAE.

Table 3: Localization accuracy and NET for interlayer options.

Resistance layer	Temp. range	No noise	40 dB	20 dB	NET range
Without resistance	298–373 K	94%	93%	61%	0.44–4.45 K
Linear resistance	298–373 K	98%	98%	94%	0.15–1.50 K
NTC (VO <sub>2</sub> )	298–373 K	98%	98%	91%	0.07–0.72 K
NTC (Ceramics)	973–1273 K	100%	100%	100%	1.49–14.93 K

Table 4: Temperature-estimation error measured by mean absolute error (MAE).

Resistance layer	Temp. range	No noise	40 dB	20 dB
Without resistance	298–373 K	0.02 K	0.48 K	3.81 K
Linear resistance	298–373 K	0.00 K	0.16 K	1.51 K
NTC (VO <sub>2</sub> )	298–373 K	0.01 K	0.23 K	1.60 K
NTC (Ceramics)	973–1273 K	0.01 K	1.83 K	16.72 K

At SNR = 20 dB, the VO<sub>2</sub> case is slightly less accurate than the linear case despite its lower NET, which is attributed to the fact that the VO<sub>2</sub> sensitivity enhancement is concentrated near the MIT rather than uniformly across the full 298–373 K range.

To interpret localization errors, we additionally compute the normalized spatial error  $d_{\text{norm}}$  from Eq. (19) for the misclassified test cases. Across our simulations, the distribution of  $d_{\text{norm}}$  for incorrect predictions concentrates below  $d_{\text{norm}} \leq 0.2$ , indicating that when the classifier is wrong, the predicted pixel is typically within 20% of the mesh diagonal from the true heat-source location (i.e., errors are predominantly near-misses rather than large jumps).

### 3. Discussion

We situate ThermoMesh within the broader idea of analog computation as a physical mapping between stimuli and measurements. This work combines the analog computing method proposed by Kendall et al. [44] with transduction mechanisms relying on phonon and electron transport. Related thermal analog-computing approaches based on heat transport have also been demonstrated using inverse-designed thermal metastructures that implement linear mappings via phonon conduction [16]. In the linear and nonlinear mea-

surement models developed in Section 2, ThermoMesh physically implements a map from a spatio-temporally sparse temperature field  $\mathbf{T}$  to boundary voltages  $\mathbf{V}$  via Seebeck transduction and an interlayer (constant  $R$  or NTC). In this sense, the mesh performs in-sensor analog computation. Interpreting the mesh as an analog computing substrate clarifies why design knobs such as interlayer thickness, resistivity-temperature parameters, and grid resolution directly shape minimum sensitivity, OMP recovery, and NET.

This viewpoint also suggests a connection to asynchronous temporal-contrast sensors such as the device of Lichtsteiner *et al.* [45]. In that work, each pixel generates address-events when the relative optical signal changes, i.e., the contrast signal is proportional to  $d \ln I_{\text{ph}}/dt$ , where  $I_{\text{ph}}$  denotes photocurrent, and the event output is realized by digital circuitry and an address-event representation (AER) interface. In ThermoMesh, an analogous event-driven interpretation could emerge from the temperature-dependent nonlinear interlayer response if one considers relative boundary-voltage changes rather than relative photocurrent changes: the relevant contrast-like quantity would be based on  $d \ln V/dt$  at the boundary channels, while the thresholding mechanism would be realized primarily by the nonlinear material response rather than by in-pixel digital circuits. This analogy suggests a plausible path toward future event-driven ThermoMesh readout.

Building on this hardware-as-computation viewpoint, the way ThermoMesh multiplexes information naturally connects to compressive sensing ideas. This work is conceptually similar to snapshot compressive imaging [46], but instead of compressing higher-dimensional information into 2D, it compresses 2D information into 1D. Classic snapshot systems multiplex a spatial field into a lower-dimensional measurement in a single shot; here, the resistive/thermoelectric network multiplexes the interior temperature field to a perimeter vector of boundary voltages. The sparsity prior on  $\mathbf{T}$  supplies the missing constraints for inversion, which explains the role of the NSP (linear case), OMP-based recovery, and the observed improvements in classification accuracy and MAE once the interlayer enhances separability at the boundary.

To move from conceptual analogy to concrete design choices, we will require a simulation workflow that captures both physics and computation. Simulating the computation carried out by a nonlinear resistive network [47, 48] provides a principled way to explore interlayer physics and geometry before fabrication. Our KCL-based assembly of node equations already yields  $\mathbf{A}$  and  $\mathbf{A}(\mathbf{T})$ ; extending this with established nonlinear network solvers enables fast, convergent updates of node potentials and currents as material laws  $\rho(T)$

and geometry parameters vary. This workflow makes it possible to sweep interlayer thickness,  $\beta$  in the NTC law, and grid size to quantify how these choices reshape minimum sensitivity, uniformity, and NET across operating regimes.

With an efficient simulator in hand, the learning rule should align with the device’s native relaxation dynamics. Training the network as an energy-based model using Equilibrium Propagation [49] aligns naturally with the device physics. The boundary electrodes play the role of output nodes: in the free phase they are measured while left electrically floating, and in the nudged phase they can be weakly perturbed by injected currents, while interior node voltages relax to steady states that minimize an energy functional defined by conductances and Seebeck sources. Equilibrium Propagation leverages this physical relaxation both for inference and for learning local parameters, suggesting a co-design loop in which material parameters (e.g.,  $\rho_0$ ,  $\beta$ ) and readout weights are tuned using gradient information derived from the same dynamics that govern operation. We envision the realization of this concept through hardware-in-the-loop training at the manufacturing stage.

These modeling and learning ingredients, taken together, point to a spectrum of sensing architectures that balance deterministic and random structures. In the future, we seek to discover a context-aware structured nonlinear sensing matrix [7] that lies between deterministic cross-bar array [50] designs and purely random reservoirs [51, 52]. The results in Section 2 already trace this continuum: a regular cross-bar supports analytic guarantees (e.g., NSP for  $q=1$ ), whereas measured nonlinear interlayers introduce controllable nonlinearity that improves separability under noise. Introducing mild structure in the nonlinearity (patterned thickness, graded  $\beta$ , or sparse cross-links) promises reservoir-like richness while preserving uniqueness guarantees and the low-power readout advantages of a deterministic array.

The design of the linear sensing matrix could, in principle, be formulated as a modified overcomplete dictionary-learning problem [53]—where, instead of enforcing sparsity on the input signal, we assume known input sparsity and impose structural constraints on the sensing matrix (i.e., on the sensor design).

The read-only resistive memory programmed at the manufacturing stage is conceptually identical to the Mask ROM [54] used in the early stages of digital computers. This decision is justifiable for context-specific applications and also improves the reliability of the sensor. In our setting, “programming” consists of choosing materials, thicknesses, and layouts to set the entries of  $\mathbf{A}$

once and for all. For embedded, long-lifetime deployments—where calibration drift and write-induced variability are unacceptable—this Mask-ROM-like choice trades reconfigurability for predictability, environmental robustness, and consistent sensitivity and NET over time.

After defining temporal sparsity deterministically in Section 2.1, we evaluate here whether a given sensor design is likely to satisfy a characterized temporal sparsity range under random event arrivals. Let  $N_{\max}$  denote the maximum number of simultaneous events present within a measurement window. For a sensor characterized up to temporal sparsity  $q_t^{\max}$ , an operating condition is regarded as acceptable at tolerance  $\delta$  if

$$\Pr\{N_{\max} \geq q_t^{\max} + 1\} \leq \delta, \quad (25)$$

where  $\delta$  is a user-specified overlap/failure tolerance. The key implication here is that the likelihood of violating the characterized temporal sparsity range increases with the window ratio,  $K \approx \tau_m/\tau_e$ , so longer measurement windows are more likely to contain overlapping events. This behavior is illustrated in Fig. 12 using the Poisson overlap model described in Appendix A.

For Eq. (25), Appendix A provides the explicit propagation from application statistics to temporal-sparsity tolerance. In particular, Eq. (A.1) gives  $s = P_e A_s \tau_e$ , and Eq. (A.6) then maps  $s$  and  $K$  to the overlap probability. Since  $P_e$  is application dependent, it is more informative here to invert that calculation and report the maximum areal event rate compatible with a chosen tolerance. For a contact-mode  $16 \times 16$  ThermoMesh with  $50 \mu\text{m}$  pitch, the sensing area is approximately  $A_s = (16 \times 50 \mu\text{m})^2 = 6.4 \times 10^{-7} \text{ m}^2$ . Taking  $q_t^{\max} = 1$ ,  $\tau_e \approx 1 \text{ ms}$ , and  $K = 10^6$ , Eq. (A.6) gives  $\Pr\{N_{\max} \geq 2\} \leq 1\%$  provided  $P_e \lesssim 2.2 \times 10^5 \text{ m}^{-2}\text{s}^{-1}$ . Tightening the tolerance to  $10^{-4}$  reduces this bound to  $P_e \lesssim 2.2 \times 10^4 \text{ m}^{-2}\text{s}^{-1}$ . This makes explicit how an assumed rare-event arrival rate is converted into a confidence that 1-sparse operation is satisfied.

Fig. 13 illustrates a bolometer-style realization of the sparse-event assumptions. In that non-contact mode, it is useful to view the pixel geometry through a simple fill factor,

$$\text{fill factor} = \frac{A_p}{A_s/(MN)}, \quad (26)$$

which should be large enough that the event footprint satisfies  $A_e \ll A_p$ . Thermal isolation then suppresses lateral conduction and, with  $\tau_s \ll \tau_e$ , each

event can be treated as quasi-static at the pixel level. For a  $16 \times 16$  bolometer-style array with  $A_p = (10 \mu\text{m})^2$  and a fill factor = 0.9, the sensing area is  $A_s = (MN)A_p/0.9 \approx 2.84 \times 10^{-8} \text{ m}^2$ . Using the same illustrative values  $q_t^{\text{max}} = 1$ ,  $\tau_e \approx 1 \text{ ms}$ , and  $K = 10^6$ , Eq. (A.6) gives  $P_e \lesssim 5.0 \times 10^6 \text{ m}^{-2}\text{s}^{-1}$  for  $\delta = 1\%$  and  $P_e \lesssim 5.0 \times 10^5 \text{ m}^{-2}\text{s}^{-1}$  for  $\delta = 10^{-4}$ . The smaller sensing area therefore relaxes the temporal-overlap constraint at a fixed areal event rate. Separately, because  $A_e \ll A_p$  in this bolometer limit, the fill factor also controls capture probability: for a uniformly distributed subpixel event, a 90% fill factor corresponds to an approximately 90% probability that the event lands on the active absorber within a unit cell. By contrast, in the contact-mode ThermoMesh emphasized in this work, the relevant 1-sparse condition is that the detectable heated footprint satisfy  $A_e \gg A_p$  while still exciting only one pixel. Thus, the two modes satisfy the same one-pixel-per-frame requirement through different geometries and heat-spreading physics.

As a concrete use case, the finalized  $16 \times 16$  ThermoMesh with  $50 \mu\text{m}$  junction pitch is well matched to high-temperature molten-droplet detection. For this contact-mode geometry, Eq. (A.1) directly maps the assumed droplet-arrival rate to the temporal-sparsity tolerance in Eq. (A.6); the illustrative bounds above show how a specified overlap tolerance can be converted into an allowable operating regime. Under the ceramic-NTC interlayer, the sensitivity analysis showed a substantial improvement in the minimum sensitivity under elevated-temperature conditions relative to the uniform ambient-temperature case (see Section 2). Together with the boundary-only readout and the demonstrated localization, regression, and NET performance (Tables 3–4), these results indicate that the reported design is practically useful for detecting and characterizing small, fast molten droplets in embedded or harsh environments where optical access is limited.

#### 4. Conclusions and Future Work

This paper introduced *ThermoMesh*, a passive digital—analogue thermoelectric thin-film sensor that maps a spatio-temporally sparse temperature field  $\mathbf{T}$  to boundary voltages  $\mathbf{V}$  through Seebeck transduction and a resistive interlayer. Focusing on the single-event (1-sparse) regime, we defined four performance metrics—range, efficiency, sensitivity, and accuracy—and used them to compare baseline, linear-resistive, and nonlinear-interlayer designs. In the linear regime, a constant-resistance interlayer increased the minimum

sensitivity and improved spatial uniformity. By comparison, an NTC interlayer operated as a non-ideal thermal switch and sustained higher minimum sensitivity as resolution grew, thereby preserving distinguishability at scale. The temperature-dependent nonlinear interlayer response also suggests a possible future extension toward event-driven boundary readout based on relative voltage transients. Using synthetic data generated by the measurement models, the learning pipeline achieved high localization accuracy, low MAE for temperature regression, and reduced NET. As one practical application, the reported design (e.g., a  $16 \times 16$  mesh with  $50 \mu\text{m}$  pitch and a ceramic-NTC interlayer) appears well suited to high-temperature molten-droplet detection in settings where optical access is limited. In this context, the observed *misclassifications* are typically adjacent to the true hot pixel, which is sufficient to trigger event capture, guide a localized inverse heat-conduction refinement around the impact site, and reliably estimate temperature at the correct region of interest.

Looking ahead, we will experimentally validate ThermoMesh and rigorously quantify sensor resolution, including point-spread/transfer functions and the minimum resolvable separation between two sources as a function of SNR and interlayer design, while incorporating realistic noise and parasitic interlayer capacitance into the NET analysis and end-to-end transient simulations to quantify any RC-limited effect on response time. We will exploit the temporal structure of the perimeter stream by coupling quickest change-point detection [55] for statistically grounded event triggers with inverse heat-conduction solvers for rapid physics-based refinement, enabling event-driven operation in embedded environments. On the modeling side, we will extend the nonlinear setting by coupling physics-informed machine learning [56] with emerging nonlinear compressive sensing formulations [57]. Guided by inverse modeling [58], we will expand the materials search space beyond ceramic NTCs and  $\text{VO}_2$  by incorporating high-thermopower transverse thermoelectrics, pyroelectric crystals with larger  $RC$  time constants to separate fast and slow dynamics in a material-programmed manner, analogous in spirit to recent architectural physics embeddings for multiscale dynamics [59, 60], molecular thermal switches with extreme on/off ratios, and flexible neuromorphic nanomaterials as learnable priors in the training loop [26, 61, 62, 63], thereby co-designing geometry, materials, dynamics, and readout for application-specific operating ranges under fabrication constraints.

## Appendix A. Rare-event model and window validity

To characterize random events, we model events as a homogeneous Poisson process with average areal rate  $P_e$  (units:  $\text{m}^{-2}\text{s}^{-1}$ ). The expected number of *simultaneous* ongoing events over the whole sensor at a random instant is

$$s = P_e A_s \tau_e, \quad (\text{A.1})$$

so  $s$  is the mean number of events present in a single event-length snapshot over area  $A_s$ . In a single snapshot of duration  $\tau_e$ , a homogeneous Poisson model gives

$$\Pr\{N = n\} = e^{-s} \frac{s^n}{n!}, \quad n = 0, 1, 2, \dots, \quad (\text{A.2})$$

regardless of how we choose to sample or aggregate in time. For  $s \ll 1$  we have

$$\Pr\{N = 1\} \approx s, \quad \Pr\{N \geq 2\} \approx \frac{s^2}{2} \ll s, \quad (\text{A.3})$$

so multi-event overlap is intrinsically rare when  $s$  is small.

ThermoMesh readout corresponds to a *measurement window* of length  $\tau_m$ . For a given event duration  $\tau_e$ , the ratio

$$K \approx \frac{\tau_m}{\tau_e} \quad (\text{A.4})$$

is the number of event-length segments that fit inside one measurement window. We consider the random process  $N(t)$ , the number of simultaneous active events, and define the windowed maximum

$$N_{\max} = \max_{t \in [0, \tau_m]} N(t). \quad (\text{A.5})$$

For a sensor characterized up to temporal sparsity  $q_t^{\max}$ , a window is considered *valid* if  $N_{\max} \leq q_t^{\max}$  and *invalid* if  $N_{\max} \geq q_t^{\max} + 1$ . Approximating the window as  $K$  statistically independent snapshots of duration  $\tau_e$  leads to

$$\Pr\{N_{\max} \geq q_t^{\max} + 1\} \approx 1 - \left( \sum_{n=0}^{q_t^{\max}} e^{-s} \frac{s^n}{n!} \right)^K, \quad (\text{A.6})$$

which is the invalidation (failure) probability for a sensor characterized up to temporal sparsity  $q_t^{\max}$ .

For the  $q_t^{\max} = 1$  case we define

$$P_0(K, s) = \Pr\{N_{\max} = 0\}, \quad P_1(K, s) = \Pr\{N_{\max} = 1\}, \quad P_{\geq 2}(K, s) = \Pr\{N_{\max} \geq 2\},$$

so that  $P_{\geq 2}$  is the failure probability for a sensor characterized up to temporal sparsity 1, and  $P_1$  measures the fraction of windows that are both non-empty and valid for that case.

## Acknowledgements

We thank Scott Schiffres, Dehao Liu, Wenfeng Zhao, and Bruce Murray for valuable discussions and constructive feedback on this work.

## Nomenclature

<b>A</b>	Sensitivity matrix mapping junction-temperature vector $\mathbf{T}$ to boundary-voltage vector $\mathbf{V}$
$A_e$	Event footprint area
$A_p$	Pixel (junction) transducing area
$A_s$	Total sensor (sensing) area
$d_{\text{norm}}$	Normalized Euclidean localization error
$E_s$	Readout energy required to acquire one boundary-channel voltage sample
<b>G</b>	Inter-node conductance matrix in the KCL network model
$I_{\text{ph}}$	Photocurrent used in the temporal-contrast sensor analogy
$\mathbf{I}_U, \mathbf{I}_S, \mathbf{I}_V$	Selection/reference matrices used in boundary-voltage computation
$K$	Window ratio ( $K \approx \tau_m/\tau_e$ )
$M$	Number of junction (pixel) rows in the $M \times N$ ThermoMesh grid
$N$	Number of junction (pixel) columns in the $M \times N$ ThermoMesh grid
$P_e$	Areal event rate ( $\text{events m}^{-2} \text{s}^{-1}$ )
$P_n$	Boundary-noise power used in the SNR-based noise model
$P_s$	Boundary-signal power used in the SNR-based noise model
$q_s^{\max}$	Maximum spatial sparsity level up to which the sensor is characterized

$q_t^{\max}$	Maximum temporal sparsity level up to which the sensor is characterized
$R$	Interlayer resistance
$s$	Poisson mean number of simultaneous ongoing events over $A_s$ in an event-length snapshot ( $s = P_e A_s \tau_e$ )
$S$	Effective Seebeck coupling coefficient(s) in the network model
$t_n$	Sampling time associated with frame index $n$
$T$	Junction temperature on the $M \times N$ grid
$\mathbf{U}$	Interior node electric potentials
$\mathbf{V}$	Measured boundary-voltage vector
$\beta$	Thermistor $\beta$ (B-parameter / beta constant) used in the exponential NTC model
$\delta$	Allowed overlap/failure probability used to evaluate whether random operating conditions satisfy the characterized temporal sparsity range
$\epsilon_0$	Permittivity of free space
$\epsilon_r$	Relative permittivity of the resistive interlayer
$\eta_{\text{ch}}$	Channel-count reduction factor
$\kappa$	Super-linearity factor of boundary response
$\boldsymbol{\nu}$	Boundary-voltage noise vector
$\rho$	Interlayer resistivity
$\sigma$	Sensitivity (boundary-voltage swing per kelvin)
$\tau_e$	Event duration
$\tau_m$	Measurement-window duration
$\tau_s$	Pixel characteristic thermal equilibration time constant

## Abbreviations

AER	Address–event representation
EMF	Electromotive force
KCL	Kirchhoff’s current law
LSTM	Long short-term memory
MAE	Mean absolute error
MIT	Metal–insulator transition
MSE	Mean squared error
NET	Noise-equivalent temperature

NSP	Null space property
NTC	Negative temperature coefficient
OMP	Orthogonal matching pursuit
SNR	Signal-to-noise ratio

## Funding sources

This research was supported by the Seed Grant Program of the Smart Energy Transdisciplinary Area of Excellence (SE TAE) at Binghamton University.

## Declaration of Competing Interest

The authors declare that they have no known competing financial interests or personal relationships that could have appeared to influence the work reported in this paper.

## References

- [1] G. Pope, M. Lerjen, S. Müllener, S. Schläpfer, T. Walti, J. Widmer, C. Studer, Light curtain localization via compressive sensing, in: 2013 IEEE International Conference on Acoustics, Speech and Signal Processing, IEEE, 2013, pp. 2558–2562.
- [2] X. Liang, J. Tang, Y. Zhong, B. Gao, H. Qian, H. Wu, Physical reservoir computing with emerging electronics, *Nature Electronics* 7 (3) (2024) 193–206.
- [3] T. Wan, B. Shao, S. Ma, Y. Zhou, Q. Li, Y. Chai, In-sensor computing: materials, devices, and integration technologies, *Advanced materials* 35 (37) (2023) 2203830.
- [4] G. Zhao, Y. Peng, J. Zhu, X. Tang, Z. Yu, In-sensor computing ann capacitive sensors, arXiv preprint arXiv:2405.17295.
- [5] M. Lustig, D. Donoho, J. M. Pauly, Sparse mri: The application of compressed sensing for rapid mr imaging, *Magnetic Resonance in Medicine: An Official Journal of the International Society for Magnetic Resonance in Medicine* 58 (6) (2007) 1182–1195.

- [6] M.-Z. Li, L.-C. Guo, G.-L. Ding, K. Zhou, Z.-Y. Xiong, S.-T. Han, Y. Zhou, Inorganic perovskite quantum dot-based strain sensors for data storage and in-sensor computing, *ACS Applied Materials & Interfaces* 13 (26) (2021) 30861–30873.
- [7] H. Akhtar, R. Kakarala, Efficient capacitive touch sensing using structured matrices, in: *Computational Imaging XIII*, Vol. 9401, SPIE, 2015, pp. 220–228.
- [8] C. Luo, M. A. Borkar, A. J. Redfern, J. H. McClellan, Compressive sensing for sparse touch detection on capacitive touch screens, *IEEE Journal on Emerging and Selected Topics in Circuits and Systems* 2 (3) (2012) 639–648.
- [9] Z. Cao, Y. Xu, S. Yu, Z. Huang, Y. Hu, W. Lin, H. Wang, Y. Luo, Y. Zheng, Z. Chen, et al., A programmable electronic skin with event-driven in-sensor touch differential and decision-making, *Advanced Functional Materials* 35 (2) (2025) 2412649.
- [10] Y. Li, Y. Yang, C. Wang, Y. Dai, X. Yan, D. Kong, Z. Liao, S. Wang, G.-J. Ruan, P. Wang, et al., Massively parallel in-sensor skinomorphic computing, *Nature Communications*.
- [11] J. Lin, C. Ma, Blind-label subwavelength ultrasound imaging, *Science Advances* 11 (5) (2025) eado2826.
- [12] J. H. Ender, On compressive sensing applied to radar, *Signal Processing* 90 (5) (2010) 1402–1414.
- [13] L. Anitori, M. Otten, P. Hoogeboom, Detection performance of compressive sensing applied to radar, *IEEE*, 2011.
- [14] H. Huang, S. Shi, J. Zha, Y. Xia, H. Wang, P. Yang, L. Zheng, S. Xu, W. Wang, Y. Ren, et al., In-sensor compressing via programmable optoelectronic sensors based on van der waals heterostructures for intelligent machine vision, *Nature Communications* 16 (1) (2025) 3836.
- [15] J. Zhao, F. Ye, Where thermomesh meets thermonet: A machine learning based sensor for heat source localization and peak temperature estimation, *Sensors and Actuators A: Physical* 292 (2019) 30–38.

- [16] C. Silva, G. Romano, Thermal analog computing: Application to matrix-vector multiplication with inverse-designed metastructures, *Physical Review Applied* 25 (1) (2026) 014073.
- [17] L. Liu, Y. Dou, J. Wang, Y. Zhao, W. Kong, C. Ma, D. He, H. Wang, H. Zhang, A. Chang, et al., Recent advances in flexible temperature sensors: Materials, mechanism, fabrication, and applications, *Advanced Science* 11 (36) (2024) 2405003.
- [18] J. A. Hidalgo-López, J. Romero-Sánchez, R. Fernández-Ramos, J. F. Martín-Canales, J. F. Ríos-Gómez, A low-cost, high-accuracy temperature sensor array, *Measurement* 125 (2018) 425–431.
- [19] C.-C. Huang, Z.-K. Kao, Y.-C. Liao, Flexible miniaturized nickel oxide thermistor arrays via inkjet printing technology, *ACS applied materials & interfaces* 5 (24) (2013) 12954–12959.
- [20] D. Katerinopoulou, P. Zalar, J. Sweelssen, G. Kiriakidis, C. Rentrop, P. Groen, G. H. Gelinck, J. van den Brand, E. C. Smits, Large-area all-printed temperature sensing surfaces using novel composite thermistor materials, *Advanced Electronic Materials* 5 (2) (2019) 1800605.
- [21] G. Urban, A. Jachimowicz, F. Kohl, H. Kuttner, F. Olcaytug, H. Kamper, F. Pittner, E. Mann-Buxbaum, T. Schalkhammer, O. Prohaska, et al., High-resolution thin-film temperature sensor arrays for medical applications, *Sensors and Actuators A: Physical* 22 (1-3) (1990) 650–654.
- [22] T. Bücher, R. Huber, C. Eschenbaum, A. Mertens, U. Lemmer, H. Amrouch, Printed temperature sensor array for high-resolution thermal mapping, *Scientific reports* 12 (1) (2022) 14231.
- [23] J. Liu, Z. Li, M. Sun, L. Zhou, X. Wu, Y. Lu, Y. Shao, C. Liu, N. Huang, B. Hu, et al., Flexible bioelectronic systems with large-scale temperature sensor arrays for monitoring and treatments of localized wound inflammation, *Proceedings of the National Academy of Sciences* 121 (49) (2024) e2412423121.
- [24] T. Nakajima, T. Tsuchiya, Ultrathin highly flexible featherweight ceramic temperature sensor arrays, *ACS Applied Materials & Interfaces* 12 (32) (2020) 36600–36608.

- [25] R. C. Webb, A. P. Bonifas, A. Behnaz, Y. Zhang, K. J. Yu, H. Cheng, M. Shi, Z. Bian, Z. Liu, Y.-S. Kim, et al., Ultrathin conformal devices for precise and continuous thermal characterization of human skin, *Nature materials* 12 (10) (2013) 938–944.
- [26] A. Daus, M. Jaikissoon, A. I. Khan, A. Kumar, R. W. Grady, K. C. Saraswat, E. Pop, Fast-response flexible temperature sensors with atomically thin molybdenum disulfide, *Nano Letters* 22 (15) (2022) 6135–6140.
- [27] P. K. Yadav, I. Yadav, B. Ajitha, A. Rajasekar, S. Gupta, Y. A. K. Reddy, Advancements of uncooled infrared microbolometer materials: A review, *Sensors and Actuators A: Physical* 342 (2022) 113611.
- [28] W. Luo, S. Zhang, Y. Gao, C. Shen, Review of mechanisms and detection methods of internal short circuits in lithium-ion batteries, *Ionics* (2025) 1–20.
- [29] L. Huang, L. Liu, L. Lu, X. Feng, X. Han, W. Li, M. Zhang, D. Li, X. Liu, D. U. Sauer, et al., A review of the internal short circuit mechanism in lithium-ion batteries: Inducement, detection and prevention, *International Journal of Energy Research* 45 (11) (2021) 15797–15831.
- [30] V. Sala, A. Vandone, F. Mazzucato, M. Banfi, S. Baraldo, A. Valente, Ai-aided thermal imaging with multispectral camera for direct energy deposition, in: *2024 IEEE International Workshop on Metrology for Industry 4.0 & IoT (MetroInd4.0 & IoT)*, IEEE, 2024, pp. 150–155.
- [31] G. A. Johnson, M. M. Dolde, J. T. Zaugg, M. J. Quintana, P. C. Collins, Monitoring, modeling, and statistical analysis in metal additive manufacturing: A review, *Materials* 17 (23) (2024) 5872.
- [32] S. De Panfilis, A. Filippini, Nucleation rate of solidification probed by x-ray absorption temperature scans in undercooled liquid metals, *Journal of Applied Physics* 88 (1) (2000) 562–570.
- [33] Y. Liu, H.-Y. Cheng, J. A. Malen, F. Xiong, Thermoelectric active cooling for transient hot spots in microprocessors, *Nature Communications* 15 (1) (2024) 4275.

- [34] K. Yang, X. Chen, T. Zhu, H. Wang, W. Luo, X. Zhu, B. Tao, H. Wang, High-sensitivity atomic layer thermopile heat-flux sensor and its application in hypersonic low-density wind tunnel tests, *IEEE Transactions on Instrumentation and Measurement* 73 (2023) 1–7.
- [35] M. Shadloo, A. Hadjadj, Laminar-turbulent transition in supersonic boundary layers with surface heat transfer: a numerical study, *Numerical Heat Transfer, Part A: Applications* 72 (1) (2017) 40–53.
- [36] F. Simoens, J. Meilhan, Terahertz real-time imaging uncooled array based on antenna-and cavity-coupled bolometers, *Philosophical Transactions of the Royal Society A: Mathematical, Physical and Engineering Sciences* 372 (2012) (2014) 20130111.
- [37] B. A. Olshausen, D. J. Field, Sparse coding of sensory inputs, *Current opinion in neurobiology* 14 (4) (2004) 481–487.
- [38] C. Escure, M. Vardelle, P. Fauchais, Experimental and theoretical study of the impact of alumina droplets on cold and hot substrates, *Plasma Chemistry and Plasma Processing* 23 (2) (2003) 185–221.
- [39] C. Chen, C. Li, S. Min, Q. Guo, Z. Xia, D. Liu, Z. Ma, F. Xia, Ultrafast silicon nanomembrane microbolometer for long-wavelength infrared light detection, *Nano Letters* 21 (19) (2021) 8385–8392.
- [40] H. Choi, X. Li, Fabrication and application of micro thin film thermocouples for transient temperature measurement in nanosecond pulsed laser micromachining of nickel, *Sensors and Actuators A: Physical* 136 (1) (2007) 118–124.
- [41] D. Houivet, J. Bernard, J.-M. Haussonne, High temperature ntc ceramic resistors (ambient–1000 c), *Journal of the European Ceramic Society* 24 (6) (2004) 1237–1241.
- [42] X. Ma, X. Liu, H. Li, A. Zhang, M. Huang, Influence of oxygen flow rate on metal–insulator transition of vanadium oxide thin films grown by rf magnetron sputtering, *Applied Physics A* 123 (3) (2017) 162.
- [43] H. Cao, X. Yan, Y. Li, L. Stan, W. Chen, N. P. Guisinger, H. Zhou, D. D. Fong, Enhancing the metal–insulator transition in vo<sub>2</sub> heterostructures with graphene interlayers, *Applied Physics Letters* 121 (8).

- [44] J. D. Kendall, A. A. Conklin, R. Pantone, J. C. Nino, S. Kumar, Scalable in-memory computing architectures for sparse matrix multiplication, in: 2022 International Electron Devices Meeting (IEDM), IEEE, 2022, pp. 21–6.
- [45] P. Lichtsteiner, C. Posch, T. Delbruck, A  $128 \times 128$  120 db 15  $\mu$ s latency asynchronous temporal contrast vision sensor, IEEE journal of solid-state circuits 43 (2) (2008) 566–576.
- [46] X. Yuan, D. J. Brady, A. K. Katsaggelos, Snapshot compressive imaging: Theory, algorithms, and applications, IEEE Signal Processing Magazine 38 (2) (2021) 65–88.
- [47] B. Scellier, A fast algorithm to simulate nonlinear resistive networks, arXiv preprint arXiv:2402.11674.
- [48] B. Scellier, S. Mishra, Universal approximation theorem for nonlinear resistive networks, Physical Review Applied 23 (4) (2025) 044009.
- [49] J. Kendall, R. Pantone, K. Manickavasagam, Y. Bengio, B. Scellier, Training end-to-end analog neural networks with equilibrium propagation. arxiv 2020, arXiv preprint arXiv:2006.01981.
- [50] F. Aguirre, A. Sebastian, M. Le Gallo, W. Song, T. Wang, J. J. Yang, W. Lu, M.-F. Chang, D. Ielmini, Y. Yang, et al., Hardware implementation of memristor-based artificial neural networks, Nature communications 15 (1) (2024) 1974.
- [51] R. Zhu, S. Lilak, A. Loeffler, J. Lizier, A. Stieg, J. Gimzewski, Z. Kuncic, Online dynamical learning and sequence memory with neuromorphic nanowire networks, Nature Communications 14 (1) (2023) 6697.
- [52] Z. Qi, L. Mi, H. Qian, W. Zheng, Y. Guo, Y. Chai, Physical reservoir computing based on nanoscale materials and devices, Advanced Functional Materials 33 (43) (2023) 2306149.
- [53] V. M. Patel, R. Chellappa, Sparse representations, compressive sensing and dictionaries for pattern recognition, in: The first Asian conference on pattern recognition, IEEE, 2011, pp. 325–329.

- [54] Y. Leblebici, S.-M. Kang, CMOS digital integrated circuits: analysis and design, McGraw-Hill New York, 1996.
- [55] Y. Xie, J. Huang, R. Willett, Change-point detection for high-dimensional time series with missing data, *IEEE Journal of Selected Topics in Signal Processing* 7 (1) (2012) 12–27.
- [56] G. E. Karniadakis, I. G. Kevrekidis, L. Lu, P. Perdikaris, S. Wang, L. Yang, Physics-informed machine learning, *Nature Reviews Physics* 3 (6) (2021) 422–440.
- [57] T. Blumensath, Compressed sensing with nonlinear observations and related nonlinear optimization problems, *IEEE Transactions on Information Theory* 59 (6) (2013) 3466–3474.
- [58] Z. Liu, M. Cai, S. Hong, J. Shi, S. Xie, C. Liu, H. Du, J. D. Morin, G. Li, L. Wang, et al., Data-driven inverse design of flexible pressure sensors, *Proceedings of the National Academy of Sciences* 121 (28) (2024) e2320222121.
- [59] M. Kohli, C. Wuethrich, K. Brooks, B. Willing, M. Forster, P. Mural, N. Setter, P. Ryser, Pyroelectric thin-film sensor array, *Sensors and Actuators A: Physical* 60 (1-3) (1997) 147–153.
- [60] H. Zhang, F. Ye, C. Ma, Physics-informed neural networks with architectural physics embedding for large-scale wave field reconstruction, *arXiv preprint arXiv:2603.02231*.
- [61] T. Feng, Z. Zhou, P. Wang, Z. Liao, Y. Wang, H. Zhao, W. Zhang, W. Liu, Transverse thermoelectric materials: Recent advances and challenges, *Next Energy* 3 (2024) 100105.
- [62] M. Li, H. Wu, E. M. Avery, Z. Qin, D. P. Goronzy, H. D. Nguyen, T. Liu, P. S. Weiss, Y. Hu, Electrically gated molecular thermal switch, *Science* 382 (6670) (2023) 585–589.
- [63] G. Ding, H. Li, J. Zhao, K. Zhou, Y. Zhai, Z. Lv, M. Zhang, Y. Yan, S.-T. Han, Y. Zhou, Nanomaterials for flexible neuromorphics, *Chemical reviews* 124 (22) (2024) 12738–12843.

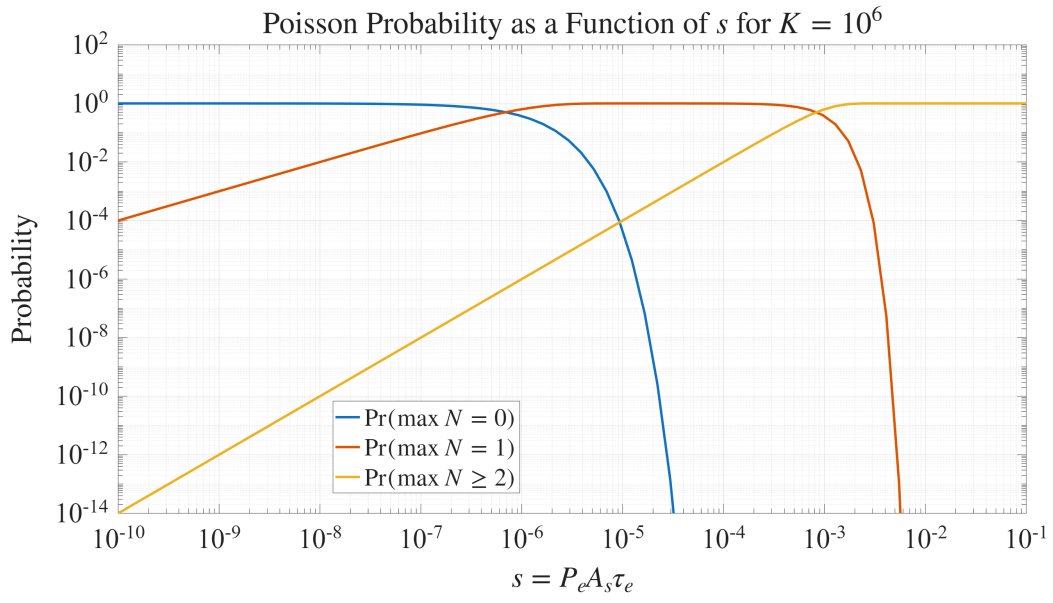
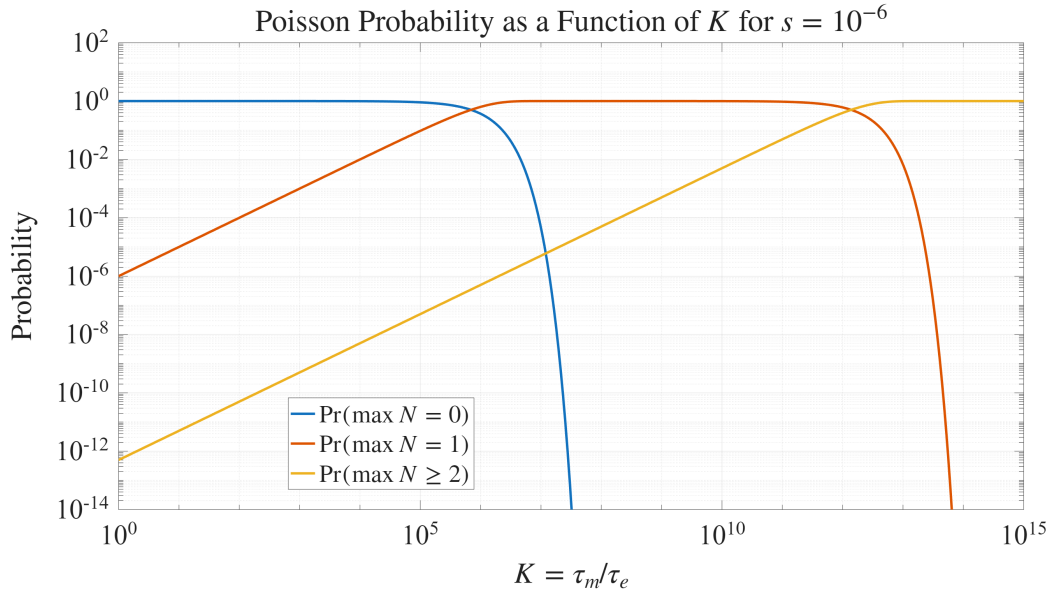


Figure 12: **Windowed Poisson overlap model.** Probabilities that the *maximum* number of simultaneous events within a measurement window is 0, 1, or  $\geq 2$ . (a) Dependence on the window ratio  $K = \tau_m/\tau_e$  for a fixed Poisson mean  $s$ . (b) Dependence on the Poisson mean  $s$  for a fixed window ratio  $K$ . These curves quantify the likelihood of sparsity violation due to event overlap.

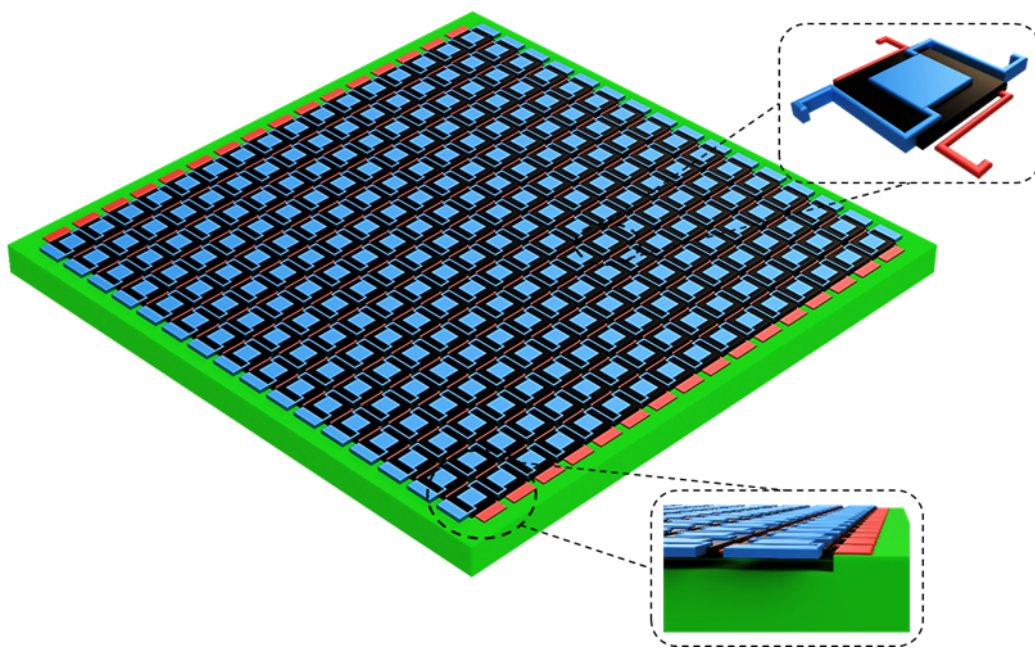


Figure 13: **Conceptual** bolometer-style isolated-pixel variant used to support effectively 1-sparse frames.